

# A rapid fine-scale approach to modelling urban bioclimatic conditions

**Journal Article****Author(s):**

Back, Yannick; Bach, Peter M.; Jasper-Tönnies, Alrun; Rauch, Wolfgang; Kleidorfer, Manfred

**Publication date:**

2021-02-20

**Permanent link:**

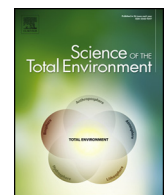
<https://doi.org/10.3929/ethz-b-000460887>

**Rights / license:**

[Creative Commons Attribution 4.0 International](#)

**Originally published in:**

Science of The Total Environment 756, <https://doi.org/10.1016/j.scitotenv.2020.143732>



## A rapid fine-scale approach to modelling urban bioclimatic conditions

Yannick Back <sup>a,\*</sup>, Peter Marcus Bach <sup>b,c</sup>, Alrun Jasper-Tönnies <sup>d</sup>, Wolfgang Rauch <sup>a</sup>, Manfred Kleidorfer <sup>a</sup>

<sup>a</sup> Unit of Environmental Engineering, University of Innsbruck, Technikerstrasse 13, 6020 Innsbruck, Austria

<sup>b</sup> Swiss Federal Institute of Aquatic Science & Technology (EAWAG), Überlandstrasse 133, 8600 Dübendorf, ZH, Switzerland

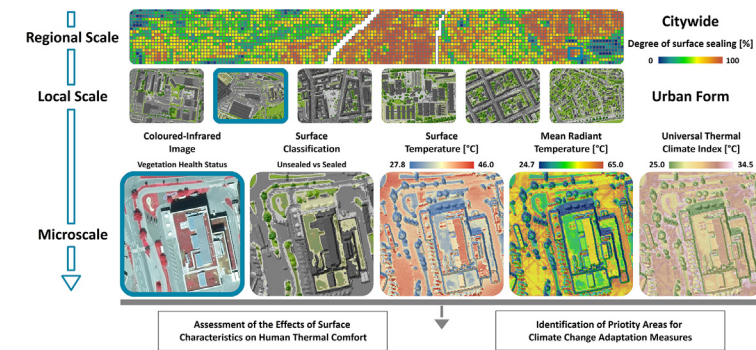
<sup>c</sup> Institute of Environmental Engineering, ETH Zürich, Zürich 8093, Switzerland

<sup>d</sup> Hydro & Meteo GmbH, Breite Strasse 6-8, 23552 Lübeck, Germany

### HIGHLIGHTS

- Fine-scale simulation of surface temperature (LST), mean radiant temperature (MRT) and UTCI
- Fast and detailed assessment of urban thermal comfort for different urban forms
- Identification of priority areas for climate change adaptation measures in urban environments
- Impact of sky view factor on calculations for bioclimatic conditions was substantial.
- High-albedo surfaces decrease LST but increase MRT and UTCI effecting human thermal comfort.

### GRAPHICAL ABSTRACT



### ARTICLE INFO

#### Article history:

Received 28 August 2020

Received in revised form 30 October 2020

Accepted 3 November 2020

Available online 25 November 2020

Editor: Jay Gan

#### Keywords:

Urban form

Heat stress

Urban amenity

Spatial modelling

Geographic Information System (GIS)

Priority areas

### ABSTRACT

Surface characteristics play a vital role in simulations for urban bioclimatic conditions. Changing relationships and distribution patterns of sealed and vegetated surfaces as well as building geometry across different scales in urban environments influence surface temperatures. Cities comprise different urban forms, which, depending on their surface characteristics, enhance the heating process, increasing the emergence of urban heat islands (UHIs). Detecting priority areas to introduce multi-beneficial climate change adaptation measures is set to be a key task for the cities long-term strategies to improve climatic conditions across different urban structures and scales. We introduce a simple and fast spatial modelling approach to carry out fine-scale simulations for land surface temperature (LST), mean radiant temperature (MRT) and Universal Thermal Climate Index (UTCI) in a 2D environment. Capabilities of our modelling approach are demonstrated in evaluating urban thermal comfort in the alpine city of Innsbruck, the capital of Tyrol in western Austria. Results show a major contrast between sealed and vegetated surfaces reflected in the distributional patterns and values of LST, MRT and UTCI, correlating with the appearance and frequency of specific surface classes. We found the Sky View Factor to have a substantial impact on calculations for bioclimatic conditions and see high-albedo surfaces decrease LST but increase the apparent temperature (MRT and UTCI values) effecting human thermal comfort. Furthermore, MRT and UTCI are more sensitive to changes in emissivity values, whereas LST is more sensitive to changes in Bowen Ratio values. Application of our modelling approach can be used to identify priority areas and maximise multi-functionality of climate change adaptation measures, to support urban planning processes for heat mitigation and the implementation of policy suggestions to achieve sustainable development goals and other political objectives.

© 2020 The Author(s). Published by Elsevier B.V. This is an open access article under the CC BY license (<http://creativecommons.org/licenses/by/4.0/>).

\* Corresponding author.

E-mail address: [Yannick.Back@uibk.ac.at](mailto:Yannick.Back@uibk.ac.at) (Y. Back).

## Nomenclature

<i>A</i>	Atmospheric radiation, [W/m <sup>2</sup> ]
<i>a<sub>k</sub></i>	Absorption coefficient of the irradiated body surface area of short-wave radiation, [/]
<i>B</i>	Soil flux, [W/m <sup>2</sup> ]
<i>B<sub>o</sub></i>	Bowen Ratio, [/]
CIR	Coloured-Infrared, [ $\mu\text{m}$ ]
DEM	Digital Elevation Model, [m]
<i>D<sub>d</sub></i>	Diffuse radiation, [W/m <sup>2</sup> ]
<i>D<sub>i</sub></i>	Direct radiation, [W/m <sup>2</sup> ]
<i>D<sub>s</sub></i>	Short-wave reflected global radiation from the surface, [W/m <sup>2</sup> ]
<i>E</i>	Long-wave radiation flux density emitted by the surface, [W/m <sup>2</sup> ]
$\varepsilon$	Surface Emissivity, [/]
$\varepsilon_p$	Emission coefficient of the human body, [/]
<i>F<sub>i</sub></i>	Solid angle portion factor, [/]
<i>f<sub>p</sub></i>	Surface projection factor, [/]
<i>G</i>	Global radiation, [W/m <sup>2</sup> ]
<i>I<sup>*</sup></i>	Radiation intensity of the sun perpendicular to the incident radiation direction, [W/m <sup>2</sup> ]
LST	Land Surface Temperature, [°C]
MRT	Mean Radiant Temperature, [°C]
<i>N</i>	Cloudiness, [Okta]
NDVI	Normalised Difference Vegetation Index, [/]
NIR	Near Infrared, [ $\mu\text{m}$ ]
<i>P<sub>Vapour</sub></i>	Water vapour pressure, [kPa]
<i>Q</i>	Net all-wave radiation flux density, [W/m <sup>2</sup> ]
<i>RH</i>	Relative Humidity, [%]
SVF	Sky View Factor, [/]
<i>T<sub>a</sub></i>	Air temperature, [°C]
<i>T<sub>MRT</sub></i>	Mean Radiant Temperature (using the 2D approach for open areas), [°C]
<i>T<sup>*</sup><sub>MRT</sub></i>	Mean Radiant Temperature (neglecting direct radiation), [°C]
<i>T<sub>MRT</sub><sup>*</sup></i>	Mean Radiant Temperature (using the SVF-approach), [°C]
<i>T<sub>s</sub></i>	Land Surface Temperature (calculated within this Study), [°C]
UTCI	Universal Thermal Climate Index, [°C]
<i>U<sub>Wind</sub></i>	Wind speed, [m/s]
VIS.G	Green portion of the visible light spectrum, [ $\mu\text{m}$ ]
VIS.R	Red portion of the visible light spectrum, [ $\mu\text{m}$ ]
<i>V<sub>p</sub></i>	Vapour pressure, [hPa]
$\sigma$	Stefan-Boltzmann constant ( $5.67 \cdot 10^{-8}$ ), [W/m <sup>2</sup> K <sup>4</sup> ]

## 1. Introduction

In the face of rapid urban and population growth, with climate change altering global and local temperature patterns and dry periods as well as the amount of Excessive Heat Events (EHE) occurring more frequently (IPCC, 2014; Gobiet et al., 2014; Chimani et al., 2016; IPCC, 2018; Bastin et al., 2019), urban planning is becoming increasingly demanding (Norton et al., 2015). Surface sealing and the decline in vegetation in cities combined with the aforementioned climatic phenomena increase the emergence of urban heat islands (UHIs), thereby adversely altering thermal comfort across districts during extreme events. Cities influence climatic conditions (e.g. air temperature, wind velocity, cloud cover, precipitation), differing from their surrounding natural and rural areas (Howard, 1833; Oke, 1982). Geometry, spacing and orientation of buildings and outdoor spaces as well as their surface characteristics are key factors for the incidence of local microclimates and the enhancement of UHIs in combination with EHEs. Sealed

surfaces (e.g. streets, concrete, roofs, parking spaces, industrial areas) can absorb a high amount of radiation, thereby heating up in the process, darker-coloured materials enhancing this process. Vegetation areas (e.g. grass, bushes, trees, parks, etc.) have different characteristics leading to a reduced heating process while receiving the same amount of radiation. Estoqué et al. (2017) examined the relationship between land surface temperature (LST), spatial pattern of sealed surfaces and green spaces. They found a strong correlation between mean LST and the density of sealed surfaces (which enhance temperatures) and green spaces (which decrease temperatures).

Changing surface characteristics affects LST distributions and, consequently, leads to changes in bioclimatic conditions and human well-being (Jenerette et al., 2016; Estoqué et al., 2017; Tran et al., 2017). To be able to assess bioclimatic conditions, various indices like the Universal Thermal Climate Index (UTCI) have been developed. Representing an equivalent temperature for a given combination of wind, radiation, humidity and air temperature (Jendritzky et al., 2012), the output depicts an assessment scale of ten categories from extreme cold stress (around  $-40^{\circ}\text{C}$ ) to extreme heat stress (above  $46^{\circ}\text{C}$ ). UTCI is capable of representing bioclimatic conditions including local characteristics and meteorological variables over time (Bröde et al., 2010; Blazejczyk et al., 2012). By comparing the UTCI to other thermal indices like the Standard Effective Temperature, Humidex, Physiological Equivalent Temperature or Wind Chill Temperature, Blazejczyk et al. (2012) found that: (1) UTCI is very sensitive to ambient changes, (2) represents specific climates, weather and locations and, most notably, (3) depicts temporal variability of thermal conditions better than other indices. The concept of UTCI calculations consists of meteorological input data, the Fiala human Physiology and Thermal Comfort (FPC) model (Fiala et al., 2010), an adaptive clothing model considering the clothing behaviour of an urban population as well as reference conditions (Bröde et al., 2013; Jendritzky et al., 2012). Having been used in many recent studies for the assessment of urban thermal stress focusing on local conditions at both larger and finer scale (e.g. Blazejczyk et al., 2014; Park et al., 2014; Ohashi et al., 2018; Kolendowicz et al., 2018; Weihs, 2019; Talhi et al., 2020), UTCI can be considered as a widely recognised state-of-the-art thermal comfort index.

UTCI calculations include Mean Radiant Temperature (MRT), which describes the radiative heat exchange between the human body and its environment, including all short- and long-wave radiation fluxes. MRT is one of the key meteorological parameters presiding over the human energy balance and the human thermal comfort (Lindberg et al., 2008) and has the strongest influence on thermo-physiological indices like the UTCI (Matzarakis et al., 2010). MRT calculations include the Stefan-Boltzmann Law, which states that the total energy radiated per unit surface area of a black body across all wavelengths per unit time is directly proportional to the fourth power of the black body's thermodynamic temperature. Therefore, LST plays an important role, influencing MRT and, consequently, UTCI calculations and values. Modelling MRT involves complex simulations (Matzarakis et al., 2010). SOLWEIG (Lindberg et al., 2008), ENVI-met (Bruse and Fleer, 1998) and RayMan (Matzarakis et al., 2010) are three common models to simulate MRT (Chen et al., 2014). All models have different approaches, carrying out simulations in a 2D or 3D environment. RayMan and SOLWEIG are freely obtainable, whereas ENVI-met is a commercial product. Additional modelling approaches to simulate certain meteorological parameters, urban microclimatic or bioclimatic conditions exist. Simulations on a 2D or 3D basis vary from: (1) using or coupling different software (Coccato et al., 2018; Leroyer et al., 2018; Broadbent et al., 2019; Oswald et al., 2019), (2) including supplementary on site measurements (Schwarz et al., 2012), (3) carrying out simulations using Computational Fluid Dynamics (CFD) software (Gromke et al., 2015; Topalar et al., 2015; Antoniou et al., 2019). CFD software enable the possibility for simulations considering detailed characteristics of the urban physics as well as essential meteorological parameters in a 3D or 2D environment (Blocken, 2015; Topalar et al., 2017). However, these simulations

are time consuming (especially with an increase in scale) and software handling still requires a significant level of expert knowledge (Parham and Haghigat, 2010; Broadbent et al., 2019). Despite these facts, complex meteorological parameters like wind velocity can be simulated and analysed using CFD software, contributing to a better understanding of the cities ventilation and its relation with the intensity of UHIs (Wong et al., 2010; Ng et al., 2011; Wong and Nichol, 2013).

Using different modelling approaches, available software and on site measurements, assessment of urban heating has been conducted in several case studies around the world, including policy approaches for adaptation (Coutts and Harris, 2013; Blazejczyk et al., 2014; Park et al., 2014; Jenerette et al., 2016; Talhi et al., 2020). Recent developments emphasise on the planning support for long-term strategies to cope with the consequences climate change poses, by identifying priority areas for decentralised stormwater systems to maximise multi-functionality (Kuller et al., 2017; Zhang and Chui, 2018; Kuller et al., 2019; Zischg et al., 2019; Bach et al., 2020).

With this modelling approach, we want to emphasise the influence that changing surface characteristics and associated surface temperatures have on bioclimatic conditions and urban heating. We present a new simple and fast spatial modelling approach that is capable of carrying out fine-scale simulations for LST, MRT and UTCI by leveraging the available accuracy from remote sensing data and the capabilities of Geographic Information System (GIS) software. Our modelling approach is based on a fine-scale surface classification embedding important surface characteristics, combined with the approach from Matzarakis et al. (2010) and Bröde et al. (2010) including essential environmental and meteorological parameters. Simulations are carried out in a 2D environment offering the opportunity for spatio-temporal evaluation of LST, MRT and UTCI distribution across different city scales. This has never been explored explicitly before. Additionally, the output raster dataset for a chosen study area includes LST, MRT and UTCI values for every single grid, only depending on three input datasets and meteorological data.

Our modelling approach enables to assess urban thermal comfort fast across different city scales and capabilities of supporting the process for heat mitigation in urban planning. We demonstrate the capabilities of our modelling approach in evaluating variable urban structure types and their potential and constraints for decentralised stormwater management based on Simperler et al. (2018)'s typology classes for the alpine city of Innsbruck, the capital of Tyrol in western Austria. These urban structures comprise different quantities of sealed and vegetated surface types, building shapes, orientation and height. Combining both approaches emphasises on the potential of multi-benefits from decentralised stormwater systems to adapt to the challenges climate change poses. Our modelling approach is capable to support urban planning for heat mitigation and the implementation of policy suggestions to achieve sustainable development goals and other political objectives.

## 2. Model overview

### 2.1. General model structure

Our fine-scale modelling approach operates on a geospatial raster with a resolution of around 0.5 m (depending on available GIS data). We use the freely available software System for Automated Geoscientific Analysis - SAGA (Conrad et al., 2015) and the commercial software ESRI ArcMap v10.6.1 (ESRI, 2019) to conduct calculations and evaluate simulation results. Apart from one metric (the Sky View Factor - SVF), which was calculated using the SAGA package, all other spatial processing and calculations were carried out in ArcMap v10.6.1 using the *Model Builder*. Two self-constructed models classify and combine the input datasets. A third self-constructed model carries out calculations.

The modelling approach follows several key steps (see Fig. 1). The first step prepares the input data comprising a digital elevation model

(DEM), coloured-infrared (CIR) image and vector layer of building geometry. From this input, we use Eq. (1) (further explained in Section 2.3) to calculate the Normalised Difference Vegetation Index (NDVI), with which we identify eight different land surface classes to which we append surface and thermal characteristics. Within a next step, conducted datasets are combined together using the tool *Combine* in ArcMap v10.6.1. This tool combines land surface classification, thermal characteristics and surface characteristics, generating one single dataset maintaining all information. From these and available meteorological data (which we append to the generated combined dataset), we then adapt the approach from Matzarakis et al. (2010) and Bröde et al. (2010) to first evaluate LST, followed by the MRT and finally the UTCI for every cell within the input raster using Eqs. (2) to (13) (further explained in Sections 2.5 and 2.6). The model's output is a fine-scale map of these three main indicators. The approach is static but can be evaluated at different times of the day as long as relevant data sets are available.

### 2.2. Input spatial and meteorological data

Three essential spatial maps are required for model input: (1) a DEM raster, (2) a CIR-image and (3) a vector layer depicting building geometry (ESRI Shapefile). The resolution of the raster datasets will determine the finest possible resolution of model output and need not be the same depending on data availability. Furthermore, the model also requires essential meteorological parameters, which are obtainable from local or regional weather stations (close to or within the simulation boundary). These parameters include air temperature ( $T_a$ ), wind speed ( $U_{Wind}$ ), vapour pressure ( $V_p$ ), cloudiness ( $N$ ) and relative humidity ( $RH$ ). Depending on data availability, one or more meteorological stations can be assigned to the simulation area or its parts. For example, in one of our applications of the model, we use 10 parameter sets from two stations representing 10 h during the diurnal cycle on a hot summer day with air temperatures exceeding 30 °C.

### 2.3. Apply surface classification

Pre-processing of input data is necessary in order to merge CIR-images and extract the input datasets for the selected study sites. Vector datasets are burnt to the input raster. To avoid areas of 'no data' due to calculations using different formats (raster- and vector-based), we use the tool *Nibble* in ArcMap v10.6.1 to replace 'no data' cells with the values of the nearest neighbour (ESRI, 2019).

The next step is the calculation of the Normalised Difference Vegetation Index (NDVI), which displays a spectrum used to classify vegetation health and density (Bhandari et al., 2012; MacFaden et al., 2012). Already in 1979, C.J. Tucker studied and introduced the relationship between leaf water content and chlorophyll content and red and photographic infrared radiances (Compton, 1979). Today, the NDVI is a well-established and widely used index in many different sectors (i.e. forestry, agriculture, urban planning, etc.) for land cover classification (Bhandari et al., 2012; Hiscock et al., 2020), urban tree canopy mapping (MacFaden et al., 2012) or crop yield estimation (Bolten and Friedl, 2013; Huang et al., 2014). As a general linear and exponential relationship between NDVI and LAI (Leaf Area Index) is existent, NDVI can also be used to rapidly and non-destructively estimate LAI indirectly (Fan et al., 2009). However, improvement in predicting LAI by NDVI is still needed (Fan et al., 2009; Viña et al., 2011). Recently, Tan et al. (2020) introduced a novel method monitoring LAI through remote sensing by integrating NDVI and Beer-Lambert law. Results show, that the modified model is better than the two individual methods, providing an improvement in predicting LAI indirectly. A relationship between NDVI and LST associated with urban land use types and patterns is also observable (Yue et al., 2007), detecting a difference in vegetation cover as the primary cause of the UHI effect (Guiling et al., 2008; Guo et al., 2015; Jain et al., 2020).

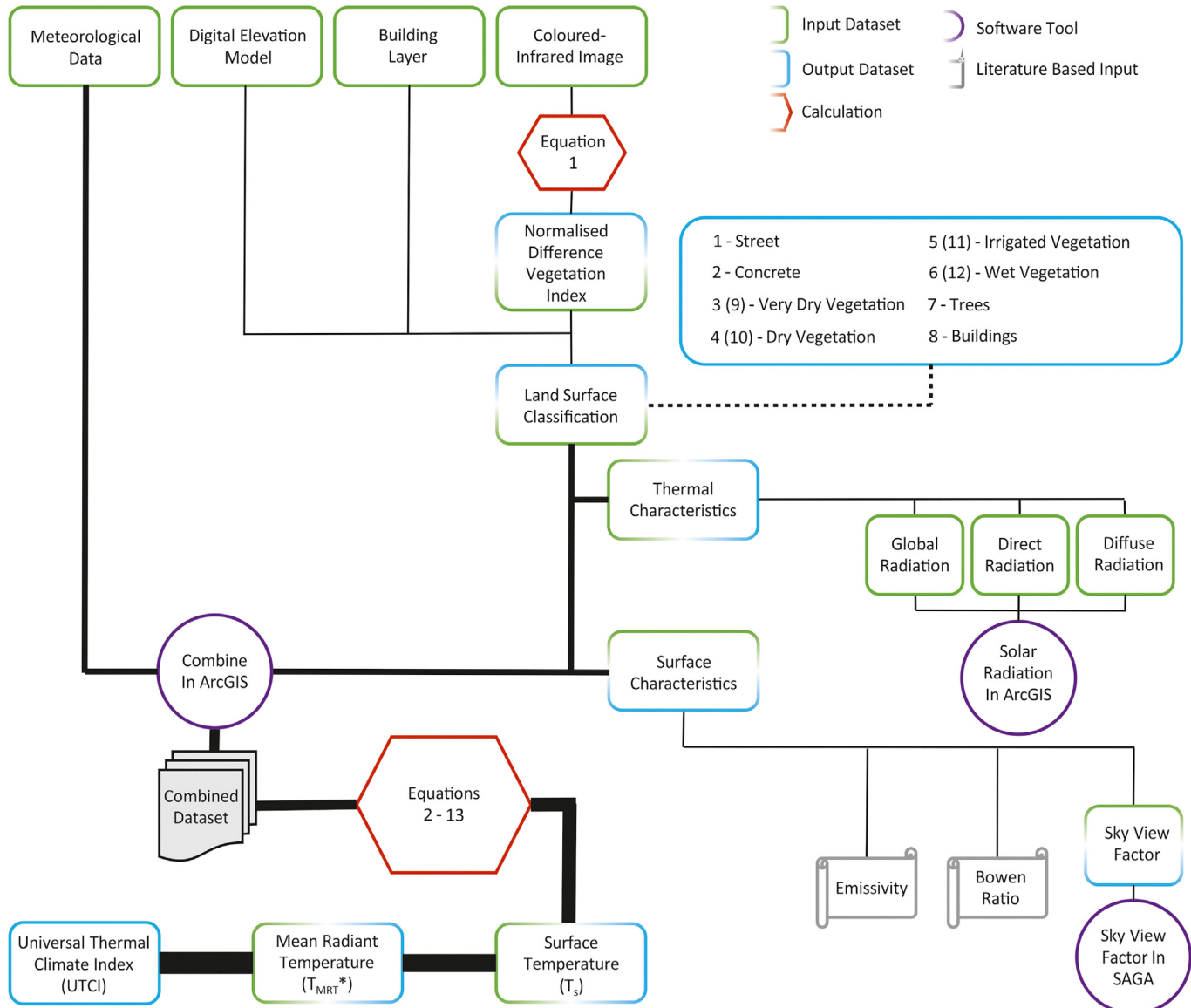


**Fig. 1.** Graphical illustration of the models key steps.

Based on a land surface classification approach after Hiscock et al. (2020), we determine the NDVI from CIR information. CIR data consists of three bands: (1) Near Infrared (NIR), (2) the red portion of the visible light spectrum (VIS.R) and (3) the green portion of the visible light spectrum (VIS.G). Using Eq. (1) (ESRI, 2019), NDVI is calculated from NIR and VIS.R information as:

$$\text{NDVI} = \frac{\text{NIR} - \text{VIS.R}}{\text{NIR} + \text{VIS.R}} \quad (1)$$

Measuring the difference between the intensities of NIR [ $\mu\text{m}$ ] and VIS.R [ $\mu\text{m}$ ], divided by the sum of these intensities, the NDVI provides values ranging from  $-1$  to  $1$ . Values above zero are typically separated into bands, which reflect the status of vegetation health (Gómez-Mendoza et al., 2008), while values close to and below zero represent non-vegetated surfaces. Water, in particular, has an NDVI value close to  $-1$ .

In our approach, the NDVI is used to distinguish between eight surface classes, which are used in the model (summarised in Table 1 with associated NDVI ranges): street, concrete, very dry vegetation, dry vegetation, irrigated vegetation, wet vegetation, trees and buildings. To

differentiate between ground and building level, we use the building layer and DEM to extract information about the vegetation health status at both levels. To distinguish between the different levels, an additional numbering is introduced (see Table 1). Numbers in brackets represent vegetation on building level. This is sometimes necessary as buildings in cities may contain green roofs, which provide a range of multiple benefits to urban residents including heat mitigation, urban amenity and stormwater management (Woods-Ballard et al., 2007; Coutts et al., 2012; Gago et al., 2013).

#### 2.4. Spatial mapping of thermal characteristics

In this step, we relate our classification to two essential parameters required for determining our output temperatures: Bowen Ratio ( $B_o$ ) and Emissivity ( $\varepsilon$ ). These properties are also necessary to weight the eight different land surface cover classes according to their characteristics in terms of vegetated and sealed surfaces (refer to Table 1).  $B_o$  describes the relationship between sensible heat and latent heat (Bowen, 1926). A change from a natural to an urban environment results in an increase of  $B_o$  values. Lower values represent wet surfaces with no sensible heat loss, whereas higher values represent dry surfaces

**Table 1**

Overview of model land surface cover classification, their associated NDVI bands, Bowen Ratios and Emissivities.

Classification	$\varepsilon$	$B_o$	NDVI Band Values
1 - Street	0.960	1.5	[−1.0, −0.08]
2 - Concrete	0.930	1.5	[−0.08, 0.01]
3 (9) - Very Dry Vegetation	0.952	0.8	[0.01, 0.15]
4 (10) - Dry Vegetation	0.962	0.5	[0.15, 0.2]
5 (11) - Irrigated Vegetation	0.976	0.2	[0.2, 0.3]
6 (12) - Wet Vegetation	0.990	0.1	[0.3, 1]
7 - Trees	0.983	0.3	[0.01, 1]
8 - Buildings	0.950	1.5	[−1, 0.01]

with no evaporation. Emissivity  $\varepsilon$  of a surface represents the effectiveness of emitting energy as thermal radiation and its ability to absorb incident radiation explained by Kirchhoff's law (Karstädt et al., 1998).  $B_o$  and  $\varepsilon$  values in our model were derived from the scientific literature (Rubio et al., 1997; Snyder et al., 1998; Bradley et al., 2002; He and Li, 2011; Coutts and Harris, 2013; EPA, 2013; Kotthaus et al., 2014; Song and Park, 2014; Humaida et al., 2016; Mandanici et al., 2016). Depending on surface classification type, we produce maps of our simulation boundary for  $B_o$  and  $\varepsilon$  values using Table 1.

Using the ArcMap's *Area Solar Radiation* tool, we then calculate global radiation ( $G$ ), direct radiation ( $D_i$ ) and diffuse radiation ( $D_d$ ) using slope and aspect information from the DEM as well as radiation parameters according to atmospheric conditions on the selected day. The tool carries out calculations based on methods from the hemispherical viewshed algorithm after Rich et al. (1994) and further developed by Fu and Rich (2000 and 2002) and implemented in ArcMap (ESRI, 2019). The outcome is a collection of raster maps comprising surface classification and characteristics  $G$ ,  $D_i$ ,  $D_d$ ,  $B_o$  and  $\varepsilon$ . We also append the necessary meteorological data to these maps (example in Table 2) and proceed to evaluate LST and bioclimatic conditions (MRT and UTCI) as outlined next. Before starting calculations, an output resolution is chosen. In this study, the input DEM has an accuracy of 0.5 m, whereas the CIR-image has an accuracy of 0.2 m. As only calculations using the ArcMap's *Area Solar Radiation* tool depend on the DEM and the parameters  $D_i$ ,  $D_d$  and  $G$  are represented in W/m<sup>2</sup>, the output resolution is set to 0.2 m.

## 2.5. Land surface temperature calculation

The calculation of land surface temperatures is based on the following Eqs. (2) to (6) after Matzarakis et al. (2010) and is dependent on the

atmospheric radiation ( $A$ ), long-wave radiation flux density emitted by the surface ( $E$ ), and the net all-wave radiation flux density ( $Q$ ). Land surface temperature  $T_s$  [°C] is defined by Eq. (2) as:

$$T_s = T_a + \frac{Q + B}{(6.2 + 4.26 \cdot U_{Wind}) \cdot \left(1 + \frac{1}{B_o}\right)} \quad (2)$$

where  $B$  is the Soil Flux [W/m<sup>2</sup>] and depends on  $Q$  defined by the relationship:

$$B = \begin{cases} -0.19 \cdot Q & Q > 0 \\ -0.32 \cdot Q & Q < 0 \end{cases} \quad (3)$$

where  $Q$  is a function of  $A$  and  $E$  and can be calculated using Eq. (4):

$$Q = a_k \cdot G + A - E \quad (4)$$

After Kirchhoff's law,  $a_k$ , the absorption coefficient of the irradiated body surface area of short-wave radiation, is replaced by  $\varepsilon$  depending on the surface classification. The relationship is implicit as  $Q$  incorporates  $E$  and  $A$ , in turn incorporates  $T_s$ , as can be seen in Eq. (5). Both values  $E$  and  $T_s$  are the two unknowns evaluated iteratively by using the system of Eqs. (2) and (5):

$$E = \varepsilon \cdot \sigma \cdot T_s^4 + (1 - \varepsilon) \cdot A \quad (5)$$

where  $\sigma$  is the Stefan-Boltzmann constant ( $5.67 \cdot 10^{-8}$  [W/m<sup>2</sup>K<sup>4</sup>]). To be able to calculate  $Q$  and solve Eq. (5),  $A$  is estimated using the following relationship:

$$A = \sigma \cdot T_a^4 \cdot \left(0.82 - 0.25 \cdot 10^{-0.0945 \cdot V_p}\right) \cdot \left(1 + 0.21 \cdot \left(\frac{N}{8}\right)^{2.5}\right) \quad (6)$$

The system of equations is solved for each cell across the map independently, producing an output of  $T_s$  that will vary across the different surface cover types.

## 2.6. Quantifying bioclimatic conditions

### 2.6.1. Mean radiant temperature calculation

In their model RayMan, Matzarakis et al. (2010) presented an approach to approximate MRT described by Eqs. (7) and (8). Eq. (7) calculates  $T^*_{MRT}$  neglecting direct radiation, whereas Eq. (8) (which incorporates Eq. (7)) calculates  $T_{MRT}$  considering direct radiation.

$$T^*_{MRT} = \left( \frac{1}{\sigma} \cdot \sum_{i=1}^n \left( E + a_k \cdot \frac{D_d}{\varepsilon_p} \right) \cdot F_i \right)^{0.25} \quad (7)$$

$T^*_{MRT}$  includes the surrounding  $n$  isothermal surfaces,  $a_k$  is the absorption coefficient of the irradiated body surface area of short-wave radiation (standard value for the human body of 0.7),  $\varepsilon_p$  is the emission coefficient of the human body (standard value of 0.97) and  $F_i$  the solid angle portion factor.

$$T_{MRT} = \left( T^*_{MRT} \cdot 4 + \frac{f_p \cdot a_k \cdot I^*}{(\varepsilon_p \cdot \sigma)} \right)^{0.25} \quad (8)$$

$T_{MRT}$  is calculated incorporating  $T^*_{MRT}$ , considering the radiation intensity of the sun on a surface perpendicular to the incident radiation direction  $I^*$  including direct radiation.  $f_p$  is the surface projection factor and is calculated using Eq. (9) depending on the elevation of the sun  $\gamma$  (Bröde, 2009).

$$f_p = 0.308 \cdot \cos \left( \gamma \cdot \frac{0.998 - \gamma^2}{48402} \right) \quad (9)$$

**Table 2**

Meteorological data from the stations in Innsbruck, University of Innsbruck Station used for case study sites IND, SHOP, TOWN and HDR, Innsbruck Airport Station used for case study sites PUB and RES.

Time	Station at the University of Innsbruck					Station at the airport of Innsbruck				
	3rd of June 2019					3rd of June 2019				
	$T_a$ [°C]	$V_p$ [hPa]	$U_{Wind}$ [m/s]	$N$ [Okta]	$RH^a$ [%]	$T_a$ [°C]	$V_p$ [hPa]	$U_{Wind}$ [m/s]	$N$ [Okta]	$RH^a$ [%]
09:00	24.2	947.0	1.4	2.0	55.40	23.1	949.6	1.1	2.0	55.40
10:00	25.8	946.4	1.5	2.0	48.92	25.3	949.0	0.6	2.0	48.92
11:00	27.6	945.7	1.0	2.0	43.48	27.1	948.2	0.3	2.0	43.48
12:00	29.2	944.9	3.5	2.0	34.77	28.3	947.5	1.6	2.0	34.77
13:00	29.7	944.3	3.4	2.0	28.48	28.9	946.8	1.7	2.0	28.48
14:00	30.2	943.6	1.3	2.0	23.87	29.2	946.2	1.9	2.0	23.87
15:00	30.0	943.0	1.2	2.0	23.47	29.4	945.5	1.8	2.0	23.47
16:00	30.0	942.9	2.4	2.0	23.88	28.2	945.4	2.9	2.0	23.88
17:00	27.7	943.0	4.8	2.0	25.35	26.3	945.5	4.5	2.0	25.35
18:00	26.1	944.1	3.5	2.0	29.60	25.5	946.5	4.5	2.0	29.60

<sup>a</sup> RH is obtained at the Unit of Environmental Engineering located close to the airport of Innsbruck.

To simulate  $T_{MRT}$  on a 2D basis we reduce the number of isothermal surfaces in Eq. (7) by using a two-directional approximation, summing up solely radiative fluxes from the surface  $\left(E + a_k \cdot \frac{D_s}{\varepsilon_p}\right)$  and the atmosphere  $\left(A + a_k \cdot \frac{D_d}{\varepsilon_p}\right)$ . Thus  $T_{MRT}$  is estimated by:

$$T_{MRT} = \left( \frac{1}{\sigma} \cdot \left( \left( E + a_k \cdot \frac{D_s}{\varepsilon_p} \right) \cdot F_s + \left( A + a_k \cdot \frac{D_d}{\varepsilon_p} \right) \cdot F_a \right) + \frac{f_p \cdot a_k \cdot I^*}{\varepsilon_p \cdot \sigma} \right)^{0.25} \quad (10)$$

where  $F_s$  and  $F_a$  are the corresponding solid angle portion factors of the ground surface and the atmosphere. This approach is different to the six-directional method, which approximates the human body as a cube and assigns different weighting coefficients to each of the six directions of short- and long-wave radiation (Chen et al., 2014). In a full 2D approach without any information about three-dimensional structures such as buildings and trees the factors  $F_s$  and  $F_a$  are set to 0.5. This is assumed to be a fairly good approximation for open areas. However, impairments in areas of an uneven terrain (e.g. street canyons surrounded by large buildings) must be accounted for.  $D_s$  in Eq. (10), is the short-wave reflected global radiation from the surface and is calculated as:

$$D_s = (1 - \varepsilon) \cdot (D_d + D_i) \quad (11)$$

Because  $F_s$  and  $F_a$  in Eq. (10) have a significant influence on  $T_{MRT}$ , we adopt a second approach to calculate  $T_{MRT}$  values, where radiative fluxes from the surface and the atmosphere are weighted based on the Sky View Factor (SVF), hence:

$$T_{MRT}^* = \left( \frac{1}{\sigma} \cdot \left( \left( E + a_k \cdot \frac{D_s}{\varepsilon_p} \right) \cdot \left( 1 - \frac{SVF}{2} \right) + \left( A + a_k \cdot \frac{D_d}{\varepsilon_p} \right) \cdot \frac{SVF}{2} \right) + \frac{f_p \cdot a_k \cdot I^*}{\varepsilon_p \cdot \sigma} \right)^{0.25} \quad (12)$$

The SVF describes the proportion of visible sky above one particular observation point. SVF values vary from 1 for completely unobstructed areas to 0 for completely obstructed areas (Böhner and Antonic, 2009). Many approaches exist to calculate the SVF for one particular point, offered for example by the model RayMan (Matzarakis et al., 2010). However, the SVF can also be stated for entire urban areas. Middel et al. (2018) presented an approach to calculate the SVF for urban areas using Google Street View. They analysed the SVF for different cities around the world and presented footprint datasets. Li et al. (2020) focused specifically on a SVF-based correlation of landscape morphology and the thermal environment of street canyons. They found a significant correlation among the SVF and temperature, relative humidity and MRT of the street canyon. For open surfaces, roofs or tree canopies the SVF is close to 1. SVF values close to 0 stand e.g. for surfaces underneath trees or within narrow street canyons. To obtain more accurate information in this regard, we calculate the SVF using the software SAGA (Conrad et al., 2015). As the algorithm of the SAGA-tool *Sky View Factor* is raster based, the tool calculates the SVF based on the DEM allowing us to append the output to the already existing raster dataset.

#### 2.6.2. Universal thermal climate index calculation

UTCI can be either determined using the FPC-model (Fiala et al., 2010) or a regression relationship. As running the thermoregulation model repeatedly is too time-consuming at the spatial resolution of our model, we calculate the UTCI as described by Bröde et al. (2012) using an approximate regression function (Eq. (13)). This relationship includes all main effects and interaction terms up to the sixth order. Embedded in the software source code provided by Bröde (2009) (available at: [http://www.utci.org/utci\\_doku.php](http://www.utci.org/utci_doku.php)), we adapted the specific part of the model's code for calculating UTCI values and included it into our calculation module. Specifically:

$$UTCI = T_a + \text{Offset}(T_a, T_{MRT}^* - T_a, U_{Wind}, P_{Vapour}) \quad (13)$$

where  $P_{Vapour}$  is the water vapour pressure [kPa] calculated using the same software source code provided by Bröde (2009). It includes a calculation procedure for saturated vapour pressure over water for input air temperature according to Hardy (1998) and requires RH as its input. The output values for  $P_{Vapour}$  will be in [hPa] and needs to be converted into [kPa] before they can be used in Eq. (13). Based on Bröde et al. (2012), the root mean squared error of this approximation is 1.1 °C.

After completing this final model step, the outputs comprise raster datasets with an accuracy <0.5 m, incorporating information about air temperature, vapour pressure, wind speed, cloudiness, surface classification, surface emissivity, Bowen ratio, global radiation, direct radiation, diffuse radiation, atmospheric radiation, long-wave radiation flux density emitted by the surface, sky view factor, surface temperature, mean radiant temperature and UTCI for every single grid of the raster dataset. This information can then be analysed further and investigated alongside other spatial data sets for the simulation region. We demonstrate this in the next sections when we apply our approach to several case study areas in Innsbruck, Austria.

### 3. Model testing & application

#### 3.1. Case study description

To cope with the challenges climate change poses, the city of Innsbruck started putting focus on implementing adaptation measures such as blue-green infrastructure or decentralised stormwater systems. Primarily designed to decouple rainwater and reduce pressure from the urban drainage system (Butler and Parkinson, 1997; Woods-Ballard et al., 2007; Torgersen et al., 2014; Mikovits et al., 2017; Goncalves et al., 2018), decentralised stormwater systems generate multi-benefits by offering infiltration, evapotranspiration and storage capabilities. Including, to a large extent, identical techniques (Fletcher et al., 2014), blue-green infrastructure and decentralised stormwater systems contribute to a reduction of sealed surfaces, consequently enhancing vegetated areas in the cities (Coutts and Harris, 2013; Gago et al., 2013; Hansen et al., 2019). These effects result in a reduction of urban heating, mitigate the UHI effect and improve bioclimatic conditions (EPA, 2008; Foster et al., 2011; Coutts et al., 2012; Jones and Somper, 2014; and Stangl et al., 2019). To prepare for future challenges, the city of Innsbruck is currently developing long-term strategies to improve climatic conditions across different urban structures. With regard to the multi-functionality of such adaptation measures, the selection of the case studies is based on the differentiation of urban structure types and their potential and constraints for decentralised stormwater management based on Simperler et al. (2018)'s typology classes. We select six unique case studies of different urban structure types in the city of Innsbruck. Fig. 2 depicts the different sites including: (IND) Operating areas and industry, (SHOP) Office administration trade and commerce, (TOWN) City centre downtown building mixed utilisation high sealing and density, (PUB) Public facilities, (HDR) Multistorey residential area with high sealing and density, (RES) Residential area with low sealing and density. These structure types exhibit different building shapes, sizes and orientations from small houses to large commercial buildings, from enclosing narrow streets to wide-open parking spaces. Furthermore, the sites differ in terms of vegetated and sealed surfaces. These specific characteristics affect the condition of urban micro- and bioclimatic conditions. Building and tree height as well as the distance between them favour the occurrence of shadows throughout the day. Shadows as well as the composition of vegetated and sealed surfaces influence surface temperatures. The chosen study sites represent typical urban structure types found in alpine cities and encompass important characteristic variations essential for microclimatic conditions.

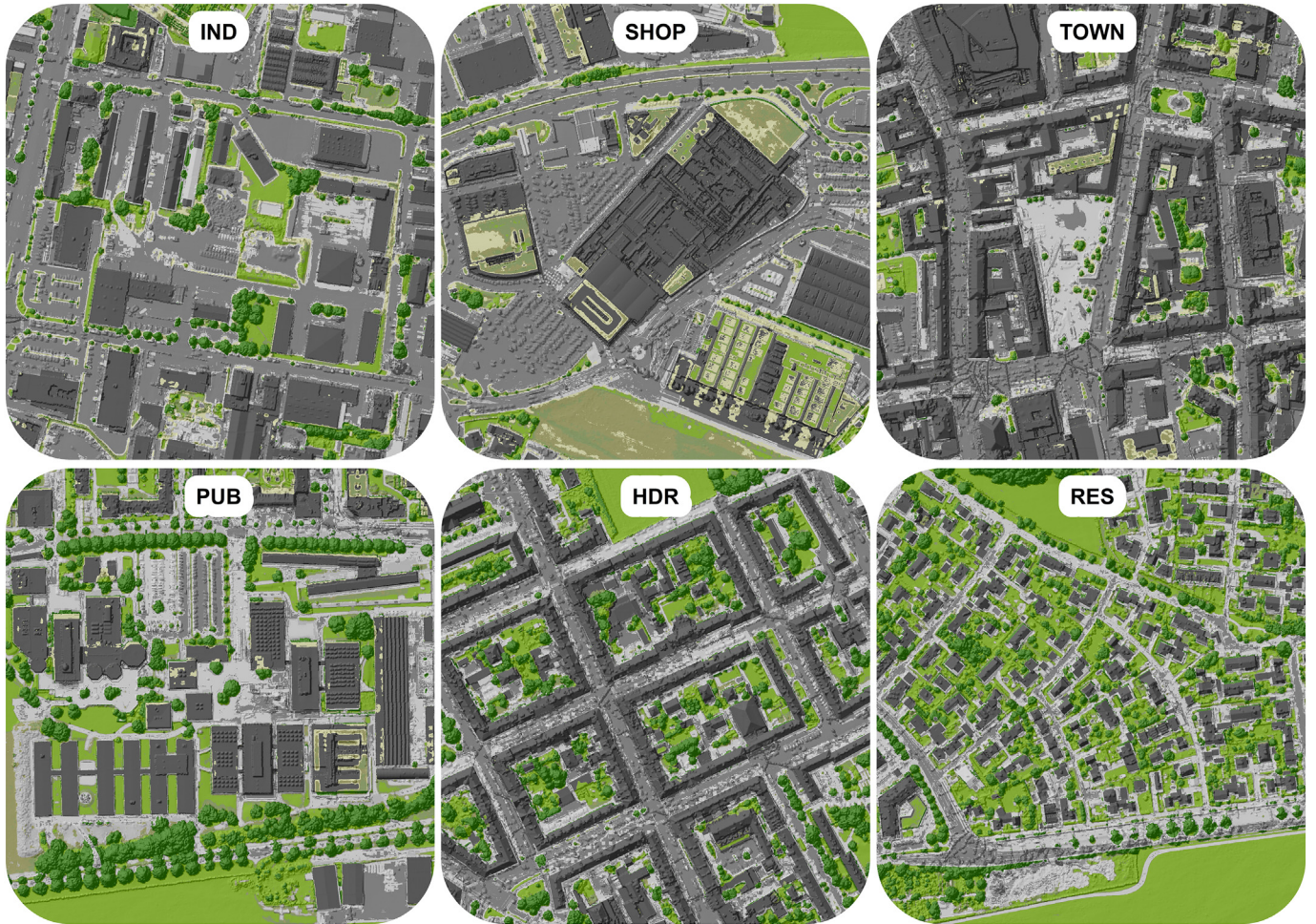


**Fig. 2.** Six different urban structure types selected after the approach of Simperler et al. (2018) for Innsbruck, Austria categorised as: (IND) Operating areas and industry, (SHOP) Office administration trade and commerce, (TOWN) city centre downtown mixed utilisation, (PUB) Public facilities, (HDR) Multi-storey residential and (RES) Residential area.

### 3.2. Data acquisition and model setup

We use a DEM raster with an accuracy of 0.5 m and a CIR-image raster with an accuracy of 0.2 m. DEM and CIR-imagery were provided by the local government Land Tirol, as is a freely available building vector layer of Tyrol (ESRI Shapefile format).

Essential meteorological parameters were obtained from two meteorological stations in Innsbruck (Station at the University of Innsbruck and Station at the airport of Innsbruck) managed by the ZAMG (Zentralanstalt für Meteorologie und Geodynamik, Innsbruck) and from one station managed by the Unit of Environmental Engineering of the University of Innsbruck (see Table 2). Due to their geographic location, we use the dataset from the station at the University of Innsbruck, located in the city centre, for sites IND, SHOP, TOWN and HDR and the dataset from the station at the airport (west of the city centre) for sites PUB and RES. RH is the only parameter obtained at the Unit of Environmental Engineering, located close to the station at the airport of Innsbruck. With the available data, we proceeded with analysing our six sites using the aforementioned methodology.

In the following Section 4, we analysed outputs of LST, MRT and UTCI across six unique urban structure types to show the capabilities of our modelling approach, evaluating: (1) the correlation between the relationship of sealed and vegetated surfaces and LST, (2) the correlation between LST and varying urban structure types, (3) diurnal LST distributions and fluctuations for 12 different surface classes, (4) distributional patterns of LST, MRT and UTCI, (5) the influence of MRT on UTCI values and (5) the correlation between LST, MRT and UTCI on a

very fine scale. These analyses were followed by an evaluation of the study results and model outputs, where we took a closer look on the effects of the SVF on MRT calculations as well as on the influence of meteorological data on the outcomes. Finally, to assure plausibility of our results, we compared the outcomes with results from the current scientific literature and discussed limitations of our modelling approach and suggestions for future studies.

## 4. Results & discussion

### 4.1. $T_s$ , $T_{MRT}^*$ and UTCI for varying urban structure types

The relationship between sealed and vegetated surfaces plays a vital role and appears differently across the six study sites (see Table 3). Table 3 shows the 12 surface classes and additionally four aggregated classes derived from the land surface classification: Sealed Surfaces, Vegetated Surfaces, Green Roofs and Buildings. It is clearly visible that none of the six structure types has a high rate of green roofs. Non-residential and high-density residential structure types (IND, SHOP, TOWN and HDR) have a high degree of sealed surfaces (close to and above 50% of the associated area). Downtown structure type (TOWN) shows a degree of vegetated surfaces below 10%, whereas public facilities (PUB) and residential areas (RES) have higher degrees of vegetated surfaces (up to 50% of the associated area).

Spatial trends are reflected in overall  $T_s$  values within the different urban structure types (see Table 3). Structure type PUB and RES with the highest degree of vegetated surfaces exhibit the lowest minimum,

**Table 3**

Percentage distribution of 12 surface classes as well as sealed surfaces, vegetated surfaces, green roofs and buildings and overall minimum, maximum and mean  $T_s$  values for the six unique urban structure types at 14:00.

	IND [%]	SHOP [%]	TOWN [%]	PUB [%]	HDR [%]	RES [%]
1 - Street	<b>44.18</b>	<b>36.66</b>	<b>31.03</b>	7.39	<b>26.27</b>	8.23
2 - Concrete	<b>11.54</b>	<b>10.84</b>	<b>16.51</b>	<b>20.73</b>	<b>14.93</b>	<b>20.85</b>
3 - Very Dry Vegetation	3.52	4.79	1.49	8.35	4.40	7.84
4 - Dry Vegetation	1.04	3.56	0.25	2.15	0.94	2.24
5 - Irrigated vegetation	2.68	4.70	0.52	3.85	1.79	5.66
6 - Wet Vegetation	4.75	8.84	1.30	9.38	6.92	<b>20.88</b>
7 - Buildings	<b>23.46</b>	<b>19.83</b>	<b>42.84</b>	<b>27.28</b>	<b>32.03</b>	<b>16.86</b>
8 - Trees	7.30	3.38	3.35	<b>18.07</b>	10.24	14.22
(9) - Very Dry Vegetation	0.49	3.50	1.37	1.79	1.76	2.46
(10) - Dry Vegetation	0.11	1.46	0.33	0.65	0.10	0.20
(11) - Irrigated vegetation	0.43	1.60	0.38	0.24	0.19	0.25
(12) - Wet Vegetation	0.50	0.83	0.64	0.11	0.44	0.38
Sealed Surfaces	55.72	47.51	47.54	28.12	41.20	29.08
Vegetated Surfaces	19.29	25.28	6.91	41.80	24.28	50.76
Green Roofs	1.53	7.38	2.72	2.80	2.49	3.29
Buildings	23.46	19.83	42.84	27.28	32.03	16.86
Minimum $T_s$	[°C]	[°C]	[°C]	[°C]	[°C]	[°C]
Maximum $T_s$	27.88	27.88	27.88	27.26	27.88	27.30
Mean $T_s$	56.47	56.47	56.41	51.73	56.56	51.81
	46.31	45.51	42.90	39.83	41.70	38.47

Numbers in bold represent the largest components across all surface classes within the different structure types.

maximum and mean  $T_s$  values. The highest mean  $T_s$  values appear in operating and industry areas (IND), where the infrastructure is planned to operate in the most productive way, forgoing the need for extensive vegetation cover and high density of buildings. Therefore, no shadows due to narrow streets or tall buildings occur and wide-open spaces allow a high penetration of radiation from the sun. Lower mean  $T_s$  in the high-density downtown (TOWN) and multi-storey residential (HDR) structure types can be explained with a higher degree of shaded surfaces caused by narrow streets and a higher number of gable roofs, thereby reducing temperatures along the faces orientated away from the sun. Additionally, the multi-storey residential (HDR) form includes inner courtyards surrounded by the building envelope. This combination increases the appearance of shadows and vegetation and, consequently, reduces temperatures.

Fig. 3 visualises the aforementioned relationship between  $T_s$  and different urban structure types. Temperature patterns and distributions can be seen in the individual maps and the associated histograms. A closer look at the histograms reveals distributional patterns towards lower  $T_s$  for urban structure types containing more vegetated surfaces (PUB and RES) or shadows (TOWN and HDR). Conversely, patterns tending towards higher temperatures can be seen in urban structure types containing a higher degree of sealed surfaces (IND and SHOP). Despite extensive shadowing and lower  $T_s$  mean values, compared to the structure types IND and SHOP, highly dense forms (TOWN and HDR) also exhibit the highest  $T_s$  values. Furthermore, histograms peak at specific temperature ranges. These peaks can be related to the occurrence and frequency of specific surface classes. Compared to the structure types IND, TOWN and HDR, offices and commerce areas (SHOP) contain the highest degree of vegetated surfaces. Consequently, specific peaks appear highest in the histogram for structure type SHOP. They point out four vegetation classes for specific temperature ranges: (1) very dry vegetation (temperature range from 47.0 °C to 48.5 °C), (2) dry vegetation (temperature range from 43.0 °C to 45.0 °C), (3) irrigated vegetation (temperature range from 37.5 °C to 39.5 °C) and (4) wet vegetation (temperature range from 33.5 °C to 35.5 °C). The highest peak exhibiting temperatures above 51 °C represents sealed surfaces. The lowest peak, exhibiting temperatures below 30.0 °C, represents shady areas. As with structure type TOWN, vegetation cover is low to negligible and peaks between the temperature extremes therefore vanish. In

this case, lower temperatures can be attributed to the appearance of shadows. The opposite is the case for structure type RES. Proportion of sealed surfaces and buildings are significantly lower, reducing the high temperature peaks. Additionally, approximately 35% of the vegetated surfaces are classified as tree or wet vegetation, leading to the disappearance of the peaks between the extreme temperatures and creating a higher peak of low temperatures. Apart from the vegetation effect, lower  $T_s$  maximum values in structure types PUB and RES can also be traced back to differences in the meteorological datasets (further explained in Section 4.2).

Fig. 4 compares diurnal  $T_s$  profiles for the different surface classes (1 to 12) shown as an example for sites SHOP and RES. These graphs not only reveal higher values for classes representing sealed surfaces but also greater diurnal fluctuations. In addition, vegetation classes representing irrigated vegetation, wet vegetation and tree clearly exhibit lower temperatures and less diurnal fluctuation compared to dry vegetation and very dry vegetation.

Surface characteristics have a strong effect on  $T_s$ ,  $T_{MRT}^*$  and UTCI values (see histograms in Fig. 3), which is consistent with previous reports (Lindberg et al., 2008; Matzarakis et al., 2010). Distributions towards extreme values, as well as particular peaks within the histograms strongly correlate to each other. In Section 4.2 Evaluation of the study results and the model output and in 4.3 Sensitivity analysis, we have a closer look on the effects of specific parameters on the target variables ( $T_s$ ,  $T_{MRT}^*$  and UTCI values).

#### 4.2. Evaluation of the study results and the model output

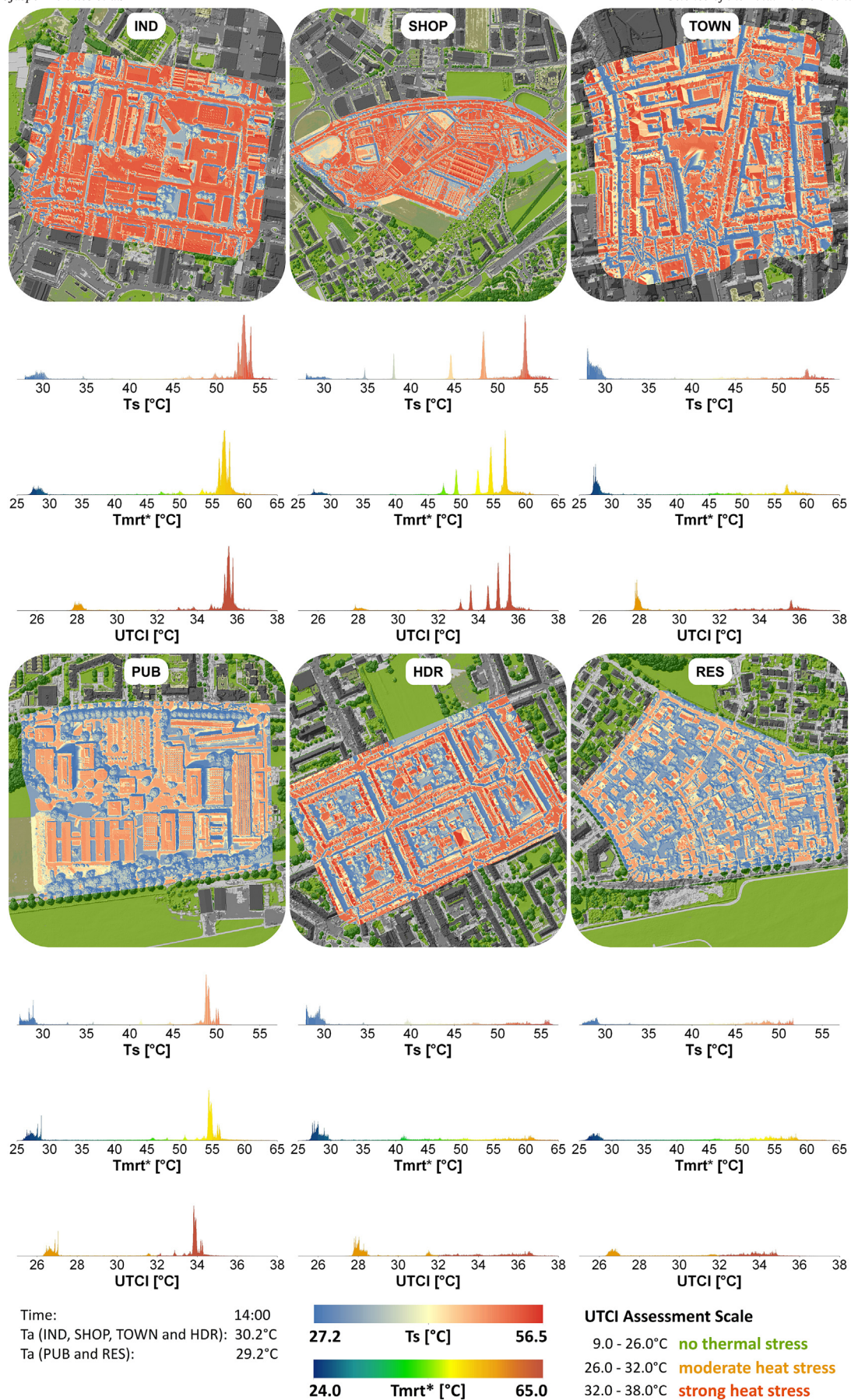
We carried out MRT calculations using the 2D approach for open areas ( $T_{MRT}$ ) and the SVF-approach ( $T_{MRT}^*$ ). Comparing the outcomes of both approaches, shows discrepancies in temperature values and distributions. With low SVF values, calculations for  $T_{MRT}^*$  are to a higher degree determined by the radiative fluxes from the surface. This leads to higher temperature values especially in obstructed areas (e.g. narrow streets). Discrepancies in temperature values can vary up to 14.3 °C, as can be seen in Fig. 5. Temperature differences mainly depend on SVF values (lower values lead to higher temperature differences) and surface classification type (low discrepancies appear on vegetated surfaces, whereas higher discrepancies appear on sealed surfaces). Using the SVF-approach increases the sensitivity of surface characteristics and its radiative fluxes.

As already mentioned in Section 4.1, different meteorological conditions in typologies PUB and RES compared to IND, SHOP, TOWN and HDR significantly influence temperature values.  $T_s$  values for structure type RES, for example, reach temperatures as high as structure type SHOP at 11:00 o'clock (shown in Fig. 4). At 14:00 o'clock, temperatures in structure type RES are lower, compared to temperatures in structure type SHOP. This can be traced back to different meteorological conditions. At 11:00 o'clock air temperatures only differ slightly from each other, but for structure type RES, wind speed was much lower. This leads to higher temperatures and extreme values in typology RES. At 14:00 o'clock air temperatures were lower and additionally wind speed was slightly higher in structure type RES. This results in lower temperatures and extreme values.

#### 4.3. Sensitivity analysis

A detailed view of the commercial and trade area (SHOP) (see Fig. 6) shows  $T_s$ ,  $T_{MRT}^*$  and UTCI values for this particular extent. Primarily, this emphasises modelling approach's capabilities to analyse LST, MRT and UTCI for numerous surface classes at a fine spatial scale. Furthermore, it shows how target variables ( $T_s$ ,  $T_{MRT}^*$  and UTCI values) are dependent on different surface classes and associated  $B_o$  and  $\varepsilon$  values, as well as by the orientation of the surface.

Specific locations are marked with a dot within the map extent of the CIR-image. The placement and numbering of dots correspond to the

**Fig. 3.**  $T_s$ ,  $T_{mrt}^*$  and UTCI distribution for different urban structure types.

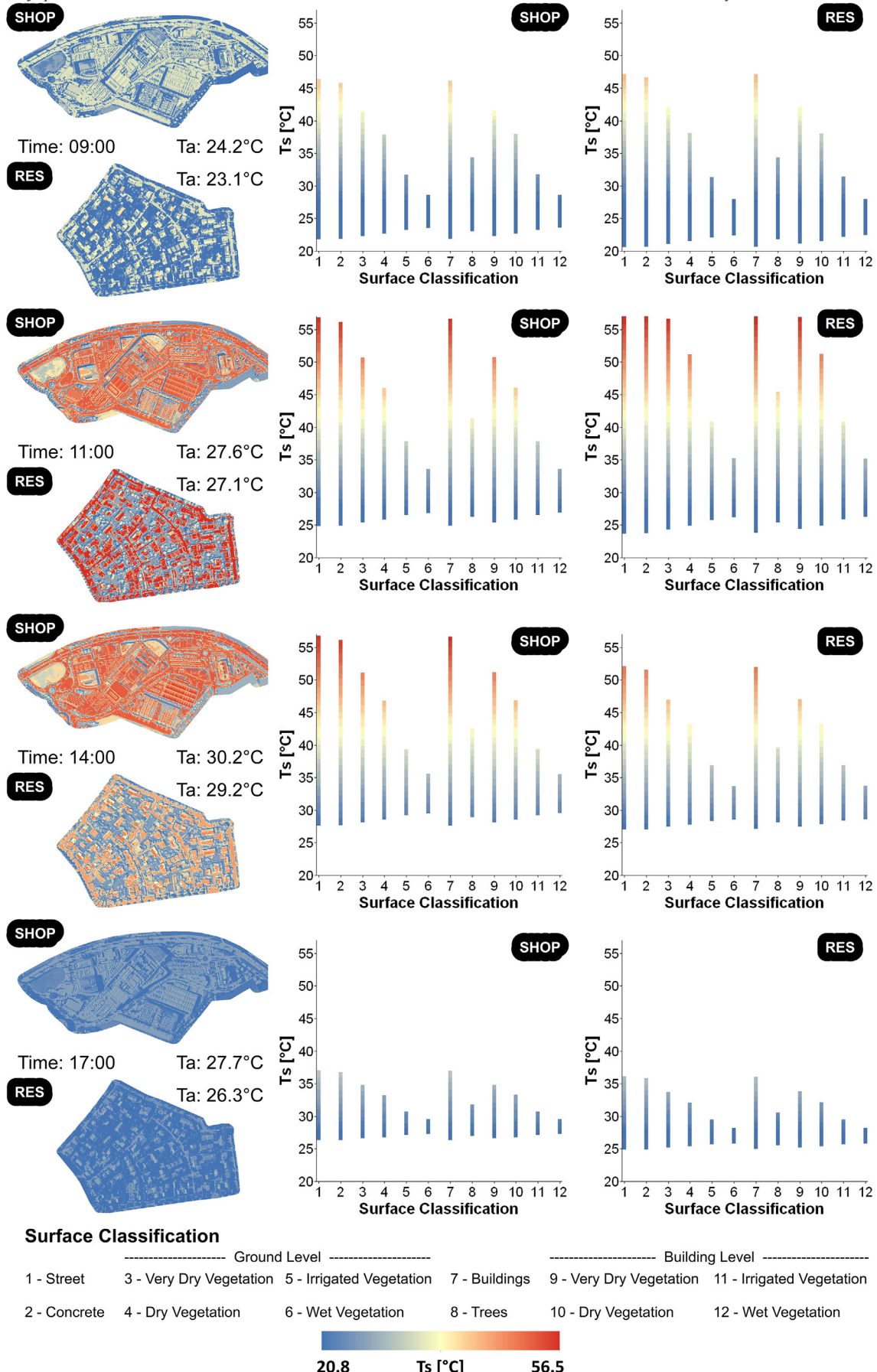


**Fig. 4.** Diurnal  $T_s$  distribution for different surface cover classes in urban typologies (SHOP) Office administration trade and commerce and (RES) Residential area.



**Fig. 5.** Differences in MRT using the 2D approach for open areas ( $T_{MRT}$ ) and the SVF-approach ( $T_{MRT}^*$ ).

surface classes (1–12). Differences in  $T_s$  values between the surface classes wet vegetation (class 6 and 12) and street (class 1) are as high as 12.7 °C. This leads to differences of 8.2 °C in  $T_{MRT}^*$  values and 2.0 °C in UTCI values respectively. Point 8 is classified as tree and is set on top of the trees canopy slightly towards the face oriented away from the sun. In addition to the effect of a low  $B_o$ , impact of shadow is also apparent in this specific example. This leads to  $T_s$  value differences of 15.4 °C between the surface class tree and the surface class street. Consequently,  $T_{MRT}^*$  value differences reach 26.5 °C, resulting in UTCI value differences of 6.6 °C. In terms of thermal stress, point 8 (class 8 – tree) can be categorised as “no thermal stress”, whereas point 1 (class 1 – street) can be categorised as “moderate heat stress”, after the UTCI assessment scale, considering environmental conditions in this example.

To emphasize on the influence  $B_o$  and  $\varepsilon$  values have on the target variables, we change the values for these parameters in the calculations for  $T_s$ ,  $T_{MRT}^*$  and UTCI, leaving all other values unchanged. Since calculating different  $B_o$  and  $\varepsilon$  values for one area would be too time consuming, we extract all necessary parameters and values from one cell and analyse changes of the target variables for one particular time step. The chosen cell is indicated with a SVF of 0.98, allowing a high amount of radiation from the sun to reach the surface. The time step is 12:00 o'clock with air temperature reaching 29.2 °C, as indicated in Fig. 6.

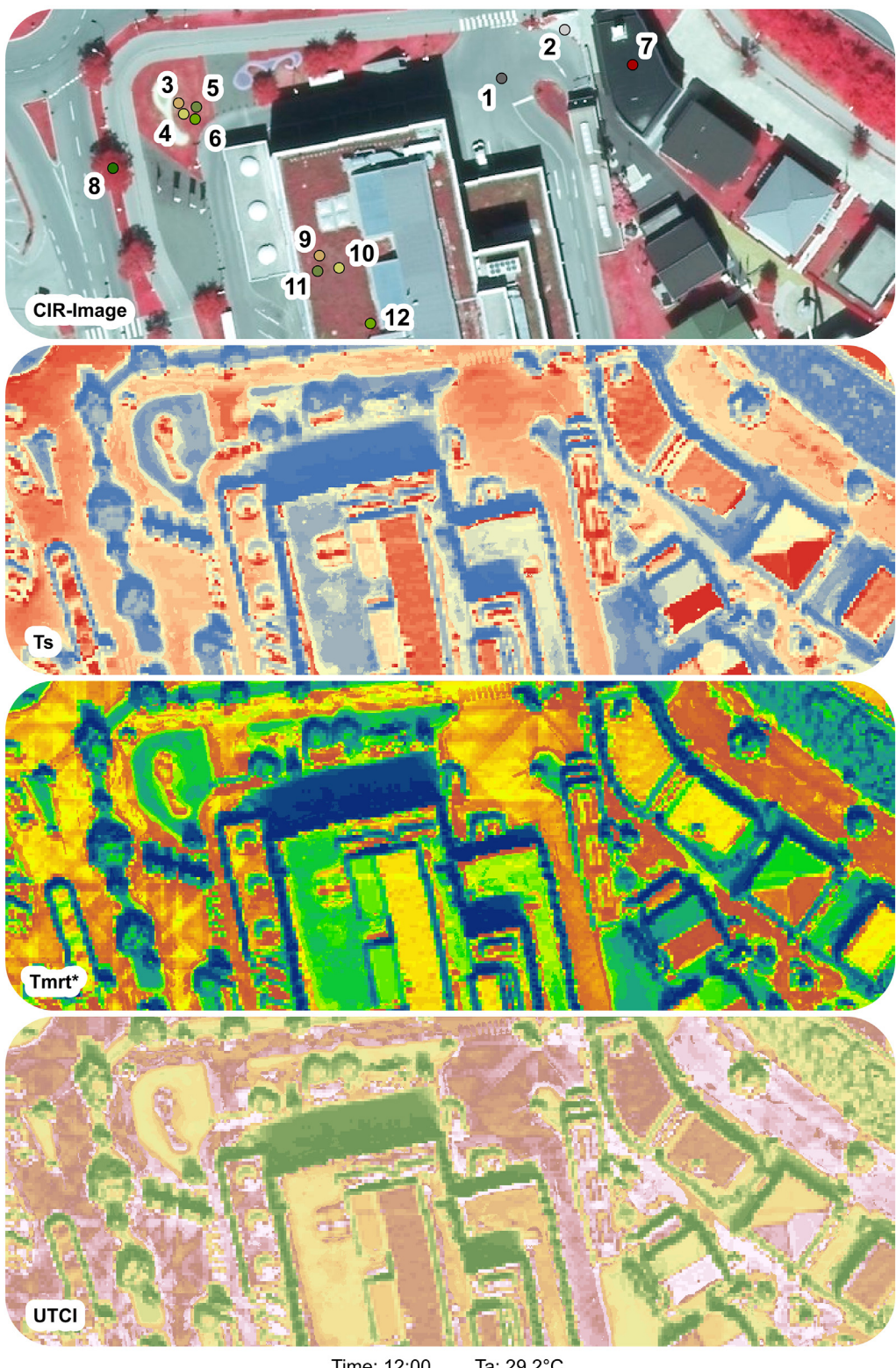
An increase of  $\varepsilon$  values describes the difference from a brighter to a darker coloured surface. An increase of  $B_o$  values describes the difference from a porous wet vegetated surface to a sealed surface. Different  $B_o$  and  $\varepsilon$  values affect  $T_s$ ,  $T_{MRT}^*$  and UTCI values differently. As was expected beforehand, an increase in  $B_o$  and/or  $\varepsilon$  values leads to an increase of  $T_s$  values and vice versa, with  $B_o$  having a greater effect (see Fig. 7).

Furthermore, with an increase of  $B_o$  values,  $T_s$  values show higher fluctuation than  $T_{MRT}^*$  and UTCI values. An increase in  $B_o$  values also increases  $T_{MRT}^*$  and UTCI.

However, the datasets also show that  $T_{MRT}^*$  and UTCI behave contrary to  $T_s$ , as these values decrease with an increase in  $\varepsilon$  and increase with a decrease in  $\varepsilon$  (see Fig. 7). The datasets show that: (1) - Brighter coloured surfaces (low  $\varepsilon$  value) do not heat up as much as darker coloured surfaces (high  $\varepsilon$  value). (2) - Brighter coloured surfaces (low  $\varepsilon$  value) reflect a high amount of short wave radiation, (3) - leading to an increase of the apparent temperature ( $T_{MRT}^*$  and UTCI values), (4) - with an increase in  $B_o$  values enhancing this process. Having a closer look at Eq. (11), an increase in  $\varepsilon$  values towards 1, will lead to a decrease of reflected short wave radiation ( $D_s$ ) towards 0. Consequently, this leads to lower  $T_{MRT}^*$  values in Eq. (12) and thus lower UTCI values in Eq. (13). (5) -  $T_{MRT}^*$  and UTCI are more sensitive to changes in  $\varepsilon$  values, whereas  $T_s$  is more sensitive to changes in  $B_o$  values.

Results in Fig. 6 also show different temperature distributions when comparing areas with flat and gable roofs. Temperatures of gable roofs change significantly depending on the position of the sun, whereas flat roofs show different temperatures depending on the vegetation availability and health. However, flat roofs without vegetation generally show lower temperatures than the sides of a gable roof facing the sun. Green roofs including healthy vegetation show lower temperatures as compared to the side of a gable roof orientated away from the sun.

These values are representative for this specific example on June 3rd at 12:00 o'clock, with an air temperature of 29.2 °C. Values and differences will definitely change depending on daytime and meteorological conditions.



Time: 12:00 Ta: 29.2°C

	1	2	3	4	5	6	7	8	9	10	11	12
Ts [°C]	44.4	43.9	40.8	33.9	34.0	31.9	44.7	29.0	41.0	38.5	33.9	31.7
Tmrt* [°C]	54.0	56.0	52.3	48.2	48.3	46.8	54.1	27.5	52.3	51.1	48.0	45.8
UTCI [°C]	32.3	32.8	31.9	30.9	30.9	30.5	32.4	25.7	31.9	31.6	30.8	30.3



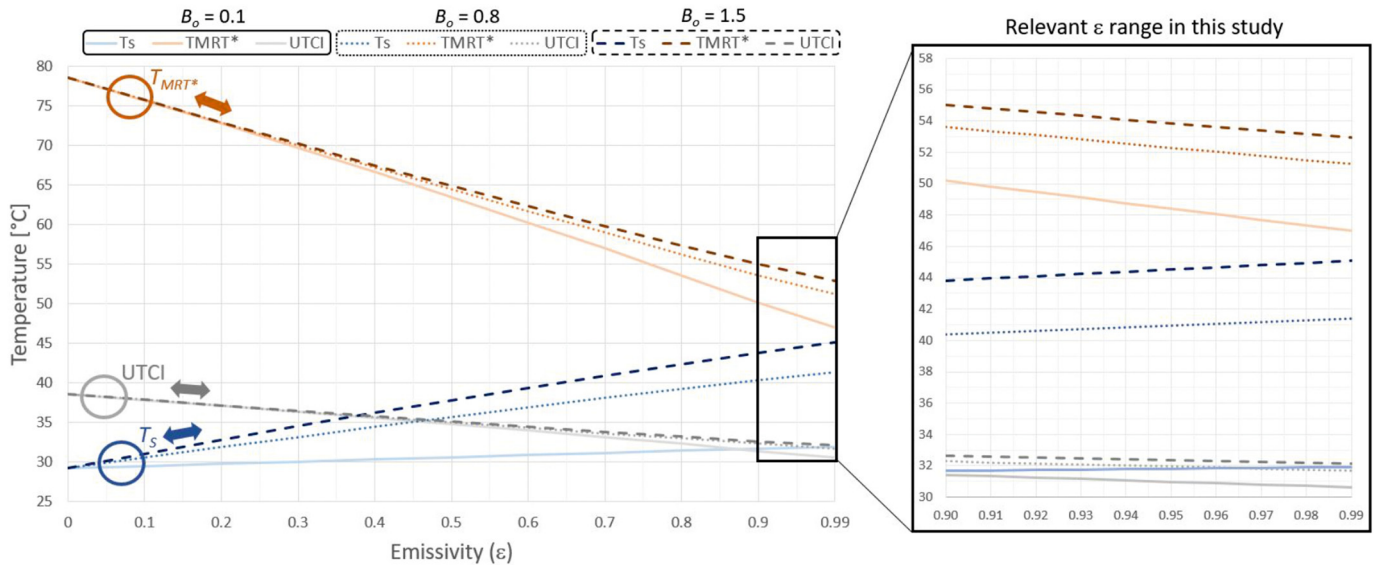


**Fig. 7.**  $T_s$ ,  $T_{MRT}^*$  and  $UTCI$  values depending on  $B_0$  and  $\epsilon$  values including a detailed extract of relevant  $\epsilon$  range in this study.

#### 4.4. Plausibility of model output

Regarding the simulation of surface temperatures, we use well-established physical relations in the model set-up, combined with accurate input datasets of spatial and meteorological data. Therefore, we have a high degree of confidence in the resulting LST. Since the conductance of highly resolved LST measurements was not within the scope of this study, we compare the range and gradients of LST output to LST measurements of previous studies conducted under similar conditions. These comprise LST measurements at the latitudinal range 46.5°–47.6° (Innsbruck: 47.3°) for the cities Basel, Switzerland and Bozen/Bolzano, Italy, at hot summer days with little cloud cover. LST simulations for Innsbruck showed values ranging from 20.8 °C up to 56.5 °C depending on surface characteristics and time of the day. Leuzinger et al. (2010) scanned parts of the city Basel from a helicopter using a high-resolution thermal camera and found LSTs ranging from 18 °C (Water) to 60 °C (buildings) with a mean air temperature during the flight of 25.1 °C. Hammerle et al. (2016) carried out LST measurements in Bozen/Bolzano, in the northern-most part of Italy investigating the atmospheric correction of landscape-scale thermography and found LSTs ranging between 10 °C and 70 °C.

Considering that our modelling approach neglects water surfaces and that the meteorological conditions vary slightly, our results show good agreement with LST values from these two studies. This is also visible when taking a closer look on different surface types. According to Leuzinger et al. (2010) the lowest values appear on water surfaces (18 °C) and shaded areas (around 22 °C). Vegetated surfaces show temperatures around 26 °C, whereas sealed surfaces show wide-spread values around 37 °C. The highest values appear on building roofs (45 °C and higher). Hammerle et al. (2016) also showed water exhibiting the lowest temperatures while the highest appeared on building roofs. While absolute values vary, we find consistent distribution patterns for different land surface types and diurnal variations in studies from other regions (Coutts and Harris, 2013; Jenerette et al., 2016). As for example, we found wet vegetation to reach lower LST values compared to dry and very dry vegetation, with a difference of 2.0 °C and 8.9 °C respectively (see Fig. 6). Analysing urban heating in Melbourne, Australia, Coutts and Harris (2013) found irrigated grass to be 3.58 °C to 5.19 °C cooler than non-irrigated grass.

Regarding MRT and UTCI, our modelling approach comprises a 2D-approximation. In contrast to LST, MRT and UTCI are derived variables and cannot be measured by airborne remote sensing. To assure the plausibility of our results, we compare the output with results from other studies using more complex modelling approaches in combination with measurements. Chen et al. (2014) compared MRT values from a field experiment and modelling in Freiburg, Germany, at 48.0° latitude. The studies were carried out in August 2010 with air temperatures exceeding 30 °C. Depending on the model (ENVI-met, SOLWEIG or RAYMAN) and on-site measurement technique, they found MRT values around 55 °C at noon. The study site was located on grass surrounded by trees and buildings. Using the SOLWEIG model, Aminipour et al. (2019) investigated MRT values across different local climate zones in Vancouver, Canada, at 49.3° latitude. During a heat wave in July 2009 with air temperatures reaching 34 °C, average MRT values ranged from 35 °C (shady areas) to 54.4 °C (exposed areas) for a period from 09:00 to 18:00 o'clock. The values from these two studies are comparable to the results from our modelling approach where MRT values range between 26 °C and 30 °C for shady areas and reach 65 °C for exposed areas. Park et al. (2014) applied the UTCI to analyse microclimatic conditions in Nanaimo, Canada, and Changwon, republic of Korea, at 49.2° and 35.2° latitude respectively. They also report values around 50 °C to 60 °C in exposed areas, 40 °C to 50 °C in narrow streets and 15 °C to 40 °C in shady areas. UTCI values for the study area in Changwon show strong heat stress (34 °C) in sunny (exposed) areas and no thermal stress (24 °C) in shady areas. In Nanaimo, the highest UTCI values occurred in the afternoon showing strong heat stress (38 °C) in sunny (exposed) areas and moderate heat stress (29 °C to 30 °C) in shady areas. These results show good agreement with UTCI values conducted using our modelling approach, with values ranging between 21 °C and 39 °C depending on surface characteristics and time of the day. Their findings also stated higher UTCI values (1 °C to 2 °C) in sunny (exposed) areas closer to building walls than farther away. This phenomenon is also visible in our results, especially for UTCI values conducted with calculations for MRT using the SVF-approach. Global radiation, approximated in our modelling approach using the tool *Area Solar Radiation* in ArcMap v10.6.1, was compared to the data sets from the ZAMG (Zentralanstalt für Meteorologie und Geodynamik, Innsbruck). When setting up the tool *Area Solar Radiation*, radiation parameters were

**Fig. 6.** Detailed View of  $T_s$ ,  $T_{MRT}^*$  and UTCI values for different surface cover classes (1–12). Placement and numbering of dots in the CIR-image correspond to the surface classes (1–12). For better visualization, we have chosen to represent UTCI values using a different colour coding than the actual UTCI assessment scale.

selected accordingly to match the global radiation values and diurnal variations recorded by the ZAMG at the two stations. Highest global radiation values in our simulations occurred at noon reaching  $965.12 \text{ W/m}^2$ . Highest global radiation values recorded by the ZAMG occurred at 11:00 o'clock reaching  $944 \text{ W/m}^2$ , whereas at noon values recorded reached  $935 \text{ W/m}^2$ .

Overall, comparison of our results with reports from the scientific literature shows a good agreement of LST, MRT and UTCI values and distributions for different land surface types as well as diurnal variations. While the evaluation of different times of the day is possible with our modelling approach, the calculation of LST, MRT and UTCI is static without interaction between different model grid cells. The model does not incorporate wind velocity simulations, simulations describing the temperature interaction between air and water as well as the horizontal heat transfer above the surface. Therefore, precise on-site measurements and further in-depth analysis are essential.

## 5. Future work and application for planning processes

Several avenues for future work exist and could include a comparison of the presented approach to more complex methods, e.g. by integrating spatially resolved datasets of the parameters wind and water, simulated using appropriate software. On-site measurements using remote thermal imagery as well as specific measurements contributing to a better understanding of different surface characteristics (e.g.  $B_0$  and  $\varepsilon$ ) within the urban areas used in this study could improve the setup, validating the modelling approach at the same time. The fact that brighter coloured surfaces (lower  $\varepsilon$  values) increase the amount

of reflected short wave radiation ( $D_s$ ) and consequently increase the apparent temperature (MRT and UTCI values), must be given more attention, as high-albedo surfaces are a common strategy for urban heat mitigation (Falasca et al., 2019). In their studies, Erell et al. (2014) and Falasca et al. (2019) already pointed out on the effect of heat stress due to high-albedo surfaces and sensitised for careful application.

We have introduced a rapid fine-scale approach to model LST, MRT and UTCI values for different urban forms. The approach is replicable and applicable in any urban environment from a small municipality to a big city, with respect to their geographic locations and climatic conditions. The approach and its results can be used to identify priority areas for adaptation measures on different scales throughout the cities and can serve as a tool for urban planners as well as for the implementation of effective policy suggestions.

At the regional scale, the surface classification used in this approach, covered with a  $50 \text{ m} \times 50 \text{ m}$  grid, can be used to identify areas with higher degree of sealed surfaces, an example of which is illustrated in Fig. 8. By extracting single areas with different degrees of surface sealing (Example 1–3 in Fig. 8), a correlation with certain urban forms can be detected. Having detected hot spots of sealed surfaces at the regional scale (in Fig. 8 an area representing the structure type SHOP was chosen), further in-depth analyses at the local scale and microscale are possible for different time steps, using the presented approach to model LST, MRT and UTCI values. Due to high accuracy in the output datasets, it is possible to analyse climate change adaptation measures e.g., occurrence, shape and vegetation health status of green roofs and detect suitable locations at the local scale and the microscale.

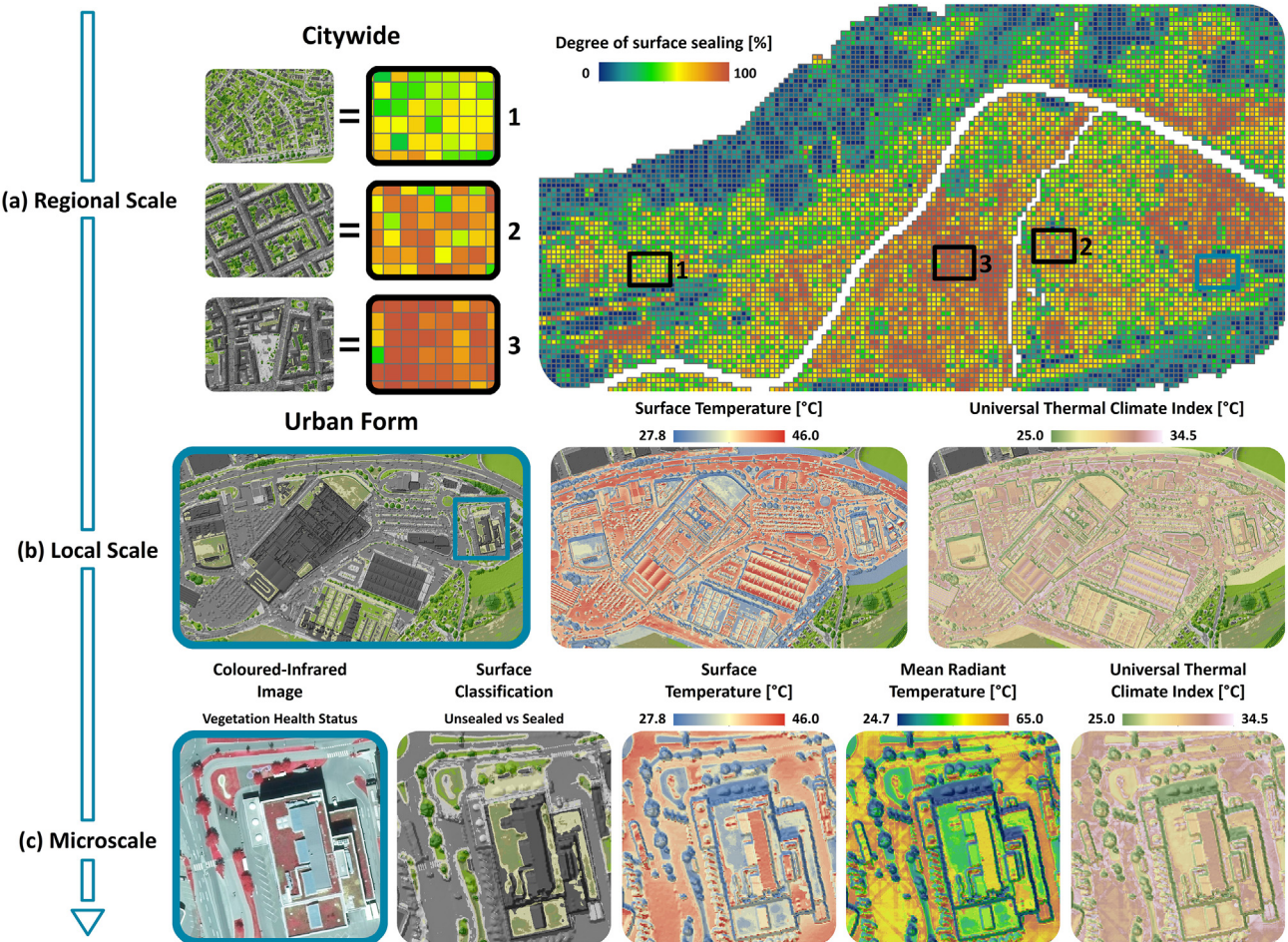


**Fig. 8.** (a) - Citywide identification of hot spots of sealed surfaces, (b) - Local in-depth analysis modelling LST, MRT and UTCI for different time steps, (c) - Fine-scale study of the area of interest.

Areas of urban thermal discomfort can be detected and suggestions for adaptation measures can be made. To enhance synergies and multiple benefits from implementing decentralised stormwater systems and blue-green infrastructure to cope with the challenges that climate change poses, we suggest combining our approach and results with approaches from different fields. For example: By combining our approach with the differentiation of urban structure types and their potential and constraints for decentralised stormwater management (e.g. Simperler et al., 2018), placement of specific decentralised stormwater techniques, offering infiltration, evapotranspiration and storage capabilities among many other ecosystem services (Kuller et al., 2017), could be optimised to mitigate urban heat and reduce pressure on the urban drainage system at the same time.

Results from our approach (and combinations with other methods from different fields) can be of high value for urban planners and for the implementation of effective policy suggestions. Hence, our approach can contribute to achieve sustainable development goals (e.g. SDG 11 - Sustainable cities and communities) in the Agenda 2030 and other political objectives (UN, 2015 and Franco et al., 2020).

## 6. Conclusion

We presented a fast and simple spatial modelling approach that is capable of carrying out fine-scale simulations for land surface temperature (LST), mean radiant temperature (MRT) and Universal Thermal Climate Index (UTCI) in a 2D environment. We demonstrated the models capabilities by simulating and evaluating these variables for varying urban structure types in the alpine city of Innsbruck, Austria. Key findings include:

- Contrasts between sealed and vegetated surfaces are reflected in surface temperatures,
- some urban typologies make up for the lack in vegetation by providing ample shading within their environment,
- distribution patterns and values of LST, MRT and UTCI across different structure types correlate with the appearance and frequency of specific surface classes,
- the effect of anthropogenic surfaces and building geometry (i.e. roof type and orientation) becomes more visible when diurnal patterns are observed,
- Sky View Factor has a substantial impact on calculations for bioclimatic conditions,
- high-albedo surfaces decrease LST but increase the apparent temperature (MRT and UTCI values) effecting human thermal comfort,
- MRT and UTCI are more sensitive to changes in emissivity values, whereas LST is more sensitive to changes in Bowen Ratio values and
- trading model complexity for a fast, simplified approach applied to a fine-scale resolution appears to be adequate in providing valuable insights about urban bioclimatic conditions.

Only minimal input data is necessary and the ability to leverage the available accuracy from remote sensing data in a Geographic Information System (GIS) software is given. The modelling approach is capable to assess urban thermal comfort fast across different city scales and to support urban planning processes for heat mitigation as well as the implementation of effective policy suggestions to achieve sustainable development goals and other political objectives. We see significant potential in applying our modelling approach to identify priority areas for adaptation measures and to maximise the multi-functionality of heat mitigation solutions such as blue-green infrastructure in urban areas.

## CRediT authorship contribution statement

**Yannick Back:** Conceptualization, Methodology, Software, Validation, Formal analysis, Investigation, Resources, Data curation, Writing -

original draft, Writing - review & editing, Visualization. **Peter Marcus Bach:** Methodology, Validation, Writing - original draft, Writing - review & editing. **Alrun Jasper-Tönnies:** Methodology, Validation, Writing - original draft, Writing - review & editing. **Wolfgang Rauch:** Resources, Writing - review & editing, Supervision. **Manfred Kleidorfer:** Resources, Writing - review & editing, Supervision, Project administration, Funding acquisition.

## Declaration of competing interest

The authors declare that they have no known competing financial interests or personal relationships that could have appeared to influence the work reported in this paper.

## Acknowledgment

This work is funded by the Austrian Climate and Energy Fund in the project: CONQUAD (Project No. KR16ACOK13143), funding period: June 2017 until October 2020 in the Austrian Climate Research Program and in the project cool-INN (Project No. KR19SCOF14953), funding period: February 2020 until January 2023 in the Smart City Demo program.

## References

- Aminipour, M., Knudby, A.J., Krayenhoff, E.S., Zickfeld, K., Middel, A., 2019. Modelling the impact of increased street tree cover on mean radiant temperature across Vancouver's local climate zones. *Urban For. Urban Green.* 39, 9–17.
- Antoniou, N., Montazeri, H., Neophytou, M., Blocken, B., 2019. CFD simulation of urban microclimate: validation using high-resolution field measurements. *Sci. Total Environ.* 695, 1–19.
- Bach, P.M., Kuller, M., McCarthy, D.T., Deletic, A., 2020. A spatial planning-support system for generating decentralised urban stormwater management schemes. *Sci. Total Environ.* 726, 138282.
- Bastin, J.-F., Clark, E., Elliott, T., Hart, S., Van den Hoogen, J., Hordijk, I., Ma, H., Majumder, S., Manoli, G., Maschler, J., Mo, L., Routh, D., Yu, K., Zohner, C.M., Crowther, T.W., 2019. Understanding climate change from a global analysis of city analogues. *PLoS One* 14 (7), 1–13.
- Bhandari, A.K., Kumar, A., Singh, G.K., 2012. Feature extraction using normalized difference vegetation index (NDVI): a case study of Jabalpur City. *Procedia Technology* 6, 612–621.
- Blazejczyk, K., Epstein, Y., Jendritzky, G., Staiger, H., Tinz, B., 2012. Comparison of UTCI to selected thermal indices. *Int. J. Biometeorol.* 56, 515–535.
- Blazejczyk, K., Kuchcik, M., Blazejczyk, A., Milewski, P., Szmyd, J., 2014. Assessment of urban thermal stress by UTCI - experimental and modelling studies: an example from Poland. *Erde* 145 (1–2), 16–33.
- Blocken, B., 2015. Computational fluid dynamics for urban physics: importance, scales, possibilities, limitations and ten tips and tricks towards accurate and reliable simulations. *Build. Environ.* 91, 219–245.
- Böhner, J., Antonic, O., Hengl, T., 2009. Land-surface parameters specific to topoclimatology. In: Reuter, H. (Ed.), *Geomorphometry – Concepts, Software, Applications. Developments in Soil Science*. vol. 33, pp. 195–226.
- Bolten, D.K., Friedl, M.A., 2013. Forecasting crop yield using remotely sensed vegetation indices and crop phenology metric. *Agric. For. Meteorol.* 173, 74–84.
- Bowen, I.S., 1926. The ratio of heat losses by conduction and by evaporation from any water surface. *Phys. Rev.* 27, 779–787.
- Bradley, A.V., Thornes, J.E., Chapman, L., Unwin, D., Roy, M., 2002. Modelling spatial and temporal road thermal climatology in rural and urban areas using GIS. *Clim. Res.* 22, 41–55.
- Broadbent, A.M., Coutts, A.M., Nice, K.A., Demuzere, M., Krayenhoff, E.S., Tapper, N.J., Wouters, H., 2019. The air-temperature response to green/blue-infrastructure evaluation tool (TARGET v1.0): an efficient and user-friendly model of city cooling. *Geoscientific Model Development* (12) 785–803.
- Bröde, Peter, 2009. UTCI universal thermal climate index documents. Available at: [http://www.utci.org/utci\\_doku.php](http://www.utci.org/utci_doku.php).
- Bröde, P., Jendritzky, G., Fiala, D., Havenith, G., 2010. The universal thermal climate index (UTCI) in operational use. *Proceedings of Conference: Adapting to Change: New Thinking on Comfort Cumberland Lodge, Windsor, UK.*
- Bröde, P., Fiala, D., Blazejczyk, K., Holmer, I., Jendritzky, G., Kampmann, B., Tinz, B., Havenith, G., 2012. Deriving the operational procedure for the Universal Thermal Climate Index (UTCI). *Int. J. Biometeorol.* 56, 481–494.
- Bröde, P., Blazejczyk, K., Fiala, D., Havenith, G., Holmer, I., Jendritzky, G., Kuklane, K., Kampmann, B., 2013. The universal thermal climate index UTCI compared to ergonomics standards for assessing the thermal environment. *Ind. Health* 51, 16–24.
- Bruse, M., Fleer, H., 1998. On the simulation of surface-plant-air interactions inside urban environments. *Environ. Model. Softw.* 13, 373–384.
- Butler, D., Parkinson, J., 1997. Towards sustainable urban drainage. *Water Sci. Technol.* 35 (9), 53–63.

- Chen, Y.-C., Lin, T.-P., Matzarakis, A., 2014. Comparison of mean radiant temperature from field experiment and modelling: a case study in Freiburg, Germany. *Theor. Appl. Climatol.* 118, 535–551.
- Chimani, B., Heinrich, G., Hostätter, M., Kerschbaumer, M., Kienberger, S., Lauprecht, A., Lexer, A., Peßenteiner, S., Poetsch, M., Salzmann, M., Spiekermann, R., Switanke, M., Truhetz, H., 2016. *Klimaszenarien für das Bundesland Tirol bis 2100. ÖKS 15 Klimasheet. Österreich.*
- Coccato, S., Pearlmutter, D., Kaempf, J., Scartezzini, J., 2018. Thermal comfort maps to estimate the impact of urban greening on the outdoor human comfort. *Urban For. Urban Green.* 35, 91–105.
- Compton, Tucker J., 1979. Red and photographic infrared linear combinations for monitoring vegetation. *Remote Sens. Environ.* 8, 127–150.
- Conrad, O., Bechtel, B., Bock, M., Dietrich, H., Fischer, E., Gerlitz, L., Wehberg, J., Wichmann, V., Böhner, J., 2015. System for Automated Geoscientific Analyses (SAGA) v.2.1.4. *Geosci. Model Dev.* (8), 1991–2007.
- Coutts, A.M., Harris, R., 2013. Watering our Cities: Urban Heat Island Report - A Multi-Scale Assessment of Urban Heating in Melbourne During an Extreme Heat Event: Policy Approaches for Adaptation. Victorian Centre for Climate Change Adaptation Research.
- Coutts, A.M., Tapper, N.J., Beringer, J., Loughnan, M., Demuzere, M., 2012. Watering our cities: the capacity for water sensitive urban design to support urban cooling and improve human thermal comfort in the Australian context. *Prog. Phys. Geogr.* 37 (1), 1–28.
- EPA - U.S. Environmental Protection Agency (2008). Reducing Urban Heat Islands: Compendium of Strategies.
- EPA - U.S. Environmental Protection Agency, 2013. *AERSURFACE User's Guide (North Carolina).*
- Erell, E., Pearlmutter, D., Boneh, D., Kutiel, P.B., 2014. Effect of high-albedo materials on pedestrian heat stress in urban street canyons. *Urban Clim.* 10 (Part 2), 367–386.
- ESRI - Environmental Systems Research Institute, 2019. *ArcGIS Desktop: Release 10. Redlands, California.*
- Estoque, R.C., Murayama, Y., Myint, S.W., 2017. Effects of landscape composition and pattern on land surface temperature: an urban heat island study in the megacities of Southeast Asia. *Sci. Total Environ.* 577, 349–359.
- Falasca, S., Ciancio, V., Salata, F., Golasi, I., Rosso, F., Curci, G., 2019. High albedo materials to counteract heat waves in cities: an assessment of meteorology, buildings energy needs and pedestrian thermal comfort. *Build. Environ.* 163, 106242.
- Fan, L., Gao, Y., Brück, H., Bernhofer, Ch., 2009. Investigating the relationship between NDVI and LAI in semi-arid grassland in Inner Mongolia using in-situ measurements. *Theor. Appl. Climatol.* 95, 151–156.
- Fiala, D., Psikuta, A., Jendritzky, G., Paulke, S., Nelson, D.A., van Marken Lichtenbelt, W.D., Frijns, A.J.H., 2010. Physiological modeling for technical, clinical and research application. *Frontiers in Bioscience (S2)* 939–968.
- Fletcher, T.D., Shuster, W., Hunt, W.F., Ashley, R., Butler, D., Arthur, S., Trowsdale, S., Barraud, S., Semadeni-Davies, A., Bertrand-Krajewski, J., Mikkelsen, P.S., Rivard, G., Uhl, M., Dagenais, D., Viklander, M., 2014. SUDS, LID, BMPs, WSUD and more - the evolution and application of terminology surrounding urban drainage. *Urban Water J.* 12 (7), 525–542.
- Foster, J., Lowe, A., Winkelman, S., 2011. *The Value of Green Infrastructure for Urban Climate Adaptation. The Centre for Clean Air Policy, Washington.*
- Franco, I.B., Chatterji, T., Derbyshire, E., Tracey, J., 2020. Actioning the Global Goals for Local Impact - Towards Sustainability Science, Policy, Education and Practice. *Science for Sustainable Societies Book Series.*
- Fu, P., Rich, P.M., 2000. *The Solar Analyst 1.0 Manual. Helios Environmental Modelling Institute (HEMI), USA.*
- Fu, P., Rich, P.M., 2002. A geometric solar radiation model with applications in agriculture and forestry. *Comput. Electron. Agric.* 37, 25–35.
- Gago, E.J., Roldan, J., Pacheco-Torres, R., Ordóñez, J., 2013. The city and urban heat islands: a review of strategies to mitigate adverse effects. *Renew. Sust. Energ. Rev.* 25, 749–758.
- Gobiet, A., Kotlarski, S., Beniston, M., Heinrich, G., Rajczak, J., Stoffel, M., 2014. 21st century climate change in the European Alps - a review. *Sci. Total Environ.* 493, 1138–1151.
- Gómez-Mendoza, L., Galicia, L., Cuevas-Fernández, M.L., Magaña, V., Gómez, G., Palacio-Prieto, J.L., 2008. Assessing onset and length of greening period in six vegetation types in Oaxaca, Mexico, using NDVI-precipitation relationships. *Int. J. Biometeorol.* 52, 511–520.
- Gonzalves, M.L.R., Zischg, J., Rau, S., Sitzmann, M., Rauch, W., Kleidorfer, M., 2018. Modeling the effects of introducing low impact development in a tropical city: a case study from Joinville, Brazil. *Sustainability* 10, 728.
- Gromke, C., Blocken, B., Janssen, W., Merema, B., van Hooff, T., Timmermans, H., 2015. CFD analysis of transpiration cooling by vegetation: case study for specific meteorological conditions during a heat wave in Arnhem, Netherlands. *Build. Environ.* 83, 11–26.
- Guiling, W., Weimei, J., Ming, W., 2008. An assessment of urban heat island effect using remote sensing data. *Mar. Sci. Bull.* 10 (2), 14–25.
- Guo, G., Wu, Z., Xiao, R., Chen, Y., Liu, X., Zhang, X., 2015. Impacts of urban biophysical composition on land surface temperature in urban heat island clusters. *Landscape Urban Plan.* 135, 1–10.
- Hammerle, A., Meier, F., Heinl, M., Egger, A., Leitinger, G., 2016. Implications of atmospheric conditions for analysis of surface temperature variability derived from landscape-scale thermography. *Int. J. Biometeorol.* 61.
- Hansen, R., Olafsson, A.S., van der Jagt, A.P.N., Rall, E., Pauleit, S., 2019. Planning multifunctional green infrastructure for compact cities: what is the state of practice? *Ecol. Indic.* 96, 99–110.
- Hardy, Bob, 1998. ITS-90 Formulations for Vapour Pressure, Frostpoint Temperature, Dewpoint Temperature, and Enhancement Factors in the Range –100 to +100 °C. the Proceedings of the Third International Symposium on Humidity & Moisture, Teddington, London.
- He, L., Li, Z., 2011. Enhancement of a fire-detection algorithm by eliminating solar contamination effects and atmospheric path radiance: application to MODIS data. *Int. J. Remote Sens.* 32, 6273–6293.
- Hiscock, O., Back, Y., Kleidorfer, M., Urich, C., 2020. A GIS-Based Land Cover Classification Approach Suitable for Fine-Scale Urban Water Management. Submitted to: Water Resources Management.
- Howard, Luke, 1833. *The Climate of London.* vol 1. International Association for Urban Climate.
- Huang, J., Wang, H., Dai, Q., Han, D., 2014. Analysis of NDVI data for crop identification and yield estimation. *IEEE Journal of selected topics in applied earth observation and remote sensing* 7 (11), 4374–4384.
- Humaida, N., Prasetyo, L.B., Rushayati, S.B., 2016. Priority assessment method of green open space (case study: Banjarbaru City). *Procedia Environ. Sci.* 33, 354–364.
- IPCC, 2014. In: Team, Core Writing, Pachauri, R.K., Meyer, L.A. (Eds.), *Climate Change 2014: Synthesis Report. Contribution of Working Groups I, II and III to the Fifth Assessment Report of the Intergovernmental Panel on Climate Change. IPCC, Geneva, Switzerland (151 pp).*
- IPCC (2018): Global Warming of 1.5°C. an IPCC Special Report on the Impacts of Global Warming of 1.5°C above Pre-Industrial Levels and Related Global Greenhouse Gas Emission Pathways, in the Context of Strengthening the Global Response to the Threat of Climate Change, Sustainable Development, and Efforts to Eradicate Poverty. [Masson-Delmotte, V., P. Zhai, H.-O. Pörtner, D. Roberts, J. Skea, P.R. Shukla, A. Pirani, W. Moufouma-Okia, C. Péan, R. Pidcock, S. Connors, J.B.R. Matthews, Y. Chen, X. Zhou, M.I. Gomis, E. Lonnoy, T. Maycock, M. Tignor, and T. Waterfield (eds.)]. (In Press).
- Jain, S., Sannigrahi, S., Sen, S., Bhattacharjee, S., Rahmat, S., 2020. Urban heat island intensity and its mitigation strategies in the fast-growing urban area. *Journal of Urban Management* 9, 54–66.
- Jendritzky, G., de Dear, R., Havenith, G., 2012. Why another thermal index? *Int. J. Biometeorol.* (56), 421–428.
- Jenerette, G.D., Harlan, S.L., Buyantuev, A., Stefanov, W.L., Declet-Barreto, J., Ruddell, B.L., Myint, S.W., Kaplan, S., li, X., 2016. Micro-scale urban surface temperatures are related to land-cover features and residential heat related health impacts in Phoenix, AZ USA. *Landsc. Ecol.* 31, 745–760.
- Jones, S., Somper, C., 2014. The role of green infrastructure in climate change adaption in London. *Geogr. J.* 180, 191–196.
- Karstädt, D., Möllmann, K., Pinno, F., Vollmer, M., 1998. *Sehen im infrarot - Grundlagen und Anwendungen der Thermographie. Physik in unserer Zeit* 29, 6–15.
- Kolendowicz, L., Polrolniczak, M., Szyska-Pluta, K., Bednorz, E., 2018. Human-biometeorological conditions in the southern Baltic coast based on the universal thermal climate index (UTCI). *Theor. Appl. Climatol.* 134, 363–379.
- Kothaus, S., Smith, T.E.L., Wooster, M.J., Grimmond, C.S.B., 2014. Derivation of an urban materials spectral library through emittance and reflectance spectroscopy. *ISPRS J. Photogramm. Remote Sens.* 94, 194–212.
- Kuller, M., Bach, P.M., Ramirez-Lovering, D., Deletic, A., 2017. Framing water sensitive urban design as part of the urban form: a critical review of tools for best planning practice. *Environ. Model Softw.* 96, 265–282.
- Kuller, M., Bach, P.M., Roberts, S., Browne, D., Deletic, A., 2019. A planning-support tool for spatial suitability assessment of green urban stormwater infrastructure. *Sci. Total Environ.* 686, 856–868.
- Leroyer, S., Belair, S., Spacek, L., Gultepe, I., 2018. Modelling of radiation-based thermal stress indicators for urban numerical weather prediction. *Urban Clim.* 25, 64–81.
- Leuzinger, S., Vogt, R., Körner, C., 2010. Tree surface temperature in an urban environment. *Agric. For. Meteorol.* 150, 56–62.
- Li, G., Ren, Z., Zhan, C., 2020. Sky view factor-based correlation of landscape morphology and the thermal environment of street canyons: a case study of Harbin, China. *Build. Environ.* 169.
- Lindberg, F., Holmer, B., Thorsson, S., 2008. SOLWEIG 1.0 - Modelling spatial variations of 3D radiant fluxes and mean radiant temperature in complex urban settings. *Int. J. Biometeorol.* 52, 697–713.
- MacFaden, S.W., O'Neil-Dunne, J.P.M., Royar, A.R., Lu, J.W.T., Rundle, A.G., 2012. High-resolution tree canopy mapping for New York City using LiDAR and object-based image analysis. *J. Appl. Remote. Sens.* 6, 1–23.
- Mandanici, E., Conte, P., Girelli, V.A., 2016. Integration of aerial thermal imagery, LiDAR data and ground surveys for surface temperature mapping in urban environments. *Remote Sens.* 8, 880–899.
- Matzarakis, A., Rutz, F., Mayer, H., 2010. Modelling radiation fluxes in simple and complex environments: basics of the RayMan model. *Int. J. Biometeorol.* 54, 131–139.
- Middel, A., Lukasczyk, J., Maciejewski, R., Demuzere, M., Roth, M., 2018. Sky view factor footprints for urban climate modelling. *Urban Clim.* 25, 120–134.
- Mikovits, C., Tscheikner-Gratl, F., Jasper-Tönnies, A., Einfalt, T., Huttonlau, M., Schöpf, M., Kinzel, H., Rauch, W., Kleidorfer, M., 2017. Decision support for adaptation planning of urban drainage systems. *J. Water Resour. Plan. Manag.* 143.
- Ng, E., Yuan, C., Chen, L., Ren, C., Fung, J.C.H., 2011. Improving the wind environment in high-density cities by understanding urban morphology and surface roughness: a study in Hong Kong. *Landscape Urban Plan.* 101, 59–74.
- Norton, B.A., Coutts, A.M., Livesley, S.J., Harris, R.J., Hunter, A.M., Williams, N.S.G., 2015. Planning for cooler cities: a framework to prioritise green infrastructure to mitigate high temperatures in urban landscapes. *Landscape Urban Plan.* 134, 127–138.
- Ohashi, Y., Katsuta, T., Tani, H., Okabayashi, T., Miyahara, S., Miyashita, R., 2018. Human cold stress of strong local-wind "Hijikawa-arashi" in Japan, based on the UTCI index and thermo-physiological responses. *Int. J. Biometeorol.* 62, 1241–1250.
- Oke, R. Timothy, 1982. The energetic basis of the urban heat island. *Q. J. R. Meteorol. Soc.* 108 (455), 1–24.

- Oswald, S., Revesz, M., Trimmel, H., Weihs, P., Zamini, S., Schneider, A., Peyerl, M., Krispel, S., Rieder, H.E., Mursch-Radlgruber, E., Lindberg, F., 2019. Coupling of urban energy balance model with 3-D radiation model to derive human thermal (dis)comfort. *Int. J. Biometeorol.* 63, 711–722.
- Parham, A.M., Haghighat, F., 2010. Approaches to study urban heat island - abilities and limitations. *Build. Environ.* 45, 2192–2201.
- Park, S., Tuller, S.E., Jo, M., 2014. Application of Universal Thermal Climate Index (UTCI) for microclimatic analysis in urban thermal environments. *Landsc. Urban Plan.* 125, 146–155.
- Rich, P.M., Dubayah, R., Hetrick, W.A., Saving, S.C., 1994. Using viewshed models to calculate intercepted solar radiation. *Applications in Ecology. American Society for Photogrammetry and Remote Sensing Technical Papers* 524–529.
- Rubio, E., Caselles, V., Badenas, C., 1997. Emissivity measurements of several soils and vegetation types in the 8–14 μm wave band: analysis of two field methods. *Remote Sens. Environ.* 59, 490–521.
- Schwarz, N., Schlink, U., Franck, U., Großmann, K., 2012. Relationship of land surface and air temperatures and its implications for quantifying urban island indicators—an application for the city of Leipzig (Germany). *Ecol. Indic.* 18, 693–704.
- Sinnerler, L., Himmelbauer, P., Stöglehner, G., Ertl, T., 2018. *Siedlungswasserwirtschaftliche Strukturtypen und ihre Potenziale für die dezentrale Bewirtschaftung von Niederschlagswasser. Österreichische Wasser- und Abfallwirtschaft* 70, 595–603.
- Snyder, W.C., Wan, Z., Zhang, Y., Feng, Y.-Z., 1998. Classification-based emissivity for land surface temperature measurement from space. *Int. J. Remote Sens.* 19, 2753–2774.
- Song, B., Park, K., 2014. Validation of ASTER surface temperature data with in situ measurements to evaluate Heat Islands in complex urban areas. *Adv. Meteorol.* 1–12.
- Stangl, R., Medl, A., Scharf, B., Pitha, U., 2019. *Wirkung der grünen Stadt - Studie zur Abbildung des aktuellen Wissenstandes im Bereich städtischer Begrünungsmaßnahmen. Für das Bundesministerium Verkehr, Innovation und Technologie, Österreich, Wien.*
- Talhi, A., Barlet, A., Bruneau, D., Aichour, B., 2020. Towards a prediction of outdoor human thermal comfort adapted for designers of urban spaces: examining UTCI and APCI in the context of Algiers (Algeria). *Int. J. Biometeorol.* 64, 651–662.
- Tan, C.-W., Zhang, P.-P., Zhou, X.-X., Wang, Z.-X., Xu, Z.-Q., Mao, W., Li, W.-X., Huo, Z.-Y., Guo, W.-S., Yun, F., 2020. Quantitative monitoring of leaf area index in wheat of different plant types by integrating NDVI and Beer-Lambert law. *Scientific Report, Nature* 10, 929.
- Toparlar, Y., Blocken, B., Vos, P., van Heijst, G.J.F., Janssen, W.D., van Hooff, T., Montazeri, H. and Timmermans, H.J.P. (2015). CFD simulation and validation of urban microclimate: a case study for Bergpolder Zuid, Rotterdam. *Build. Environ.* (83): 79–90.
- Toparlar, Y., Blocken, B., Maiheu, B., van Heijst, G.J.F., 2017. A review on the CFD analysis of urban microclimate. *Renew. Sust. Energ. Rev.* 80, 1613–1640.
- Torgersen, G., Bjerkholt, J.T., Lindholm, O.G., 2014. Addressing flooding and SuDS when improving drainage and sewerage systems - a comparative study of selected Scandinavian cities. *Water* 6, 839–857.
- Tran, D.X., Pla, F., Latorre-Carmona, P., Myint, S.W., Caetano, M., Kieu, H.V., 2017. Characterizing the relationship between land use/land cover change and land surface temperature. *ISPRS J. Photogramm. Remote Sens.* 124, 119–132.
- UN - United Nations, 2015. *Transforming our World: The 2030 Agenda for Sustainable Development. Report No. a/RES/70/1*. New York, NY.
- Viña, A., Gitelson, A.A., Nguy-Robertson, A.L., Peng, Y., 2011. Comparison of different vegetation indices for the remote assessment of green leaf area index of crops. *Remote Sens. Environ.* 115, 3468–3478.
- Weihs, P., 2019. *Influence of the Development of Outlying Districts and Urban Growth on the Urban Heat Island of the City of Vienna in the Context of Climate Change. Publizierbarer Endbericht, Klimate und Energiefonds.*
- Wong, M.S., Nichol, J.E., 2013. Spatial variability of frontal area index and its relationship with urban heat island intensity. *Int. J. Remote Sens.* 34, 885–896.
- Wong, M.S., Nichol, J.E., To, P.H., Wang, J., 2010. A simple method for designation of urban ventilation corridors and its application to urban heat island analysis. *Build. Environ.* (45), 1880–1889.
- Woods-Ballard, B., Kellagher, R., Martin, P., Jefferies, C., Bray, R., Shaffer, P., 2007. *The SuDS Manual. Published by CIRIA, London.*
- Yue, W., Xu, J., Tan, W., Xu, L., 2007. The relationship between land surface temperature and NDVI with remote sensing: application to Shanghai Landsat 7 ETM+ data. *Int. J. Remote Sens.* 28 (15), 3205–3226.
- Zhang, K., Chui, T.F.M., 2018. A comprehensive review of spatial allocation of LID-BMP-GI practices: strategies and optimization tools. *Sci. Total Environ.* 621, 915–929.
- Zischg, J., Roger, B., Gunn, A., Rauch, W., Sitzenfrei, R., 2019. Future trajectories of urban drainage systems: a simple exploratory modeling approach for assessing socio-technical transitions. *Sci. Total Environ.* 651, 1709–1719.